Astronomy & Astrophysics manuscript no. 2063 June 2, 2005
(DOI: will be inserted by hand later)

The all-sky distribution of 511 keV electron-positron annihilation emission⋆

J. Knödlseder[1], P. Jean[1], V. Lonjou[1], G. Weidenspointner[1], N. Guessoum[2], W. Gillard[1], G. Skinner[1], P. von Ballmoos[1], G. Vedrenne[1], J.-P. Roques[1], S. Schanne[3], B. Teegarden[4], V. Schönfelder[5], and C. Winkler[6]

[1] Centre d'Étude Spatiale des Rayonnements, CNRS/UPS, B.P. 4346, 31028 Toulouse Cedex 4, France
[2] American University of Sharjah, College of Arts & Science, Physics Department, PO Box 26666, Sharjah, UAE
[3] DSM/DAPNIA/SAp, CEA Saclay, 91191 Gif-sur-Yvette, France
[4] Laboratory for High Energy Astrophysics, NASA/Goddard Space Flight Center, Greenbelt, MD 20771, USA
[5] Max-Planck-Institut für Extraterrestrische Physik, Postfach 1603, 85740 Garching, Germany
[6] ESA/ESTEC, Science Operations and Data Systems Division (SCI-SD), 2201 AZ Noordwijk, The Netherlands

Received / Accepted

Abstract. We present a map of 511 keV electron-positron annihilation emission, based on data accumulated with the SPI spectrometer aboard ESA's INTEGRAL gamma-ray observatory, that covers approximately $\sim 95\%$ of the celestial sphere. Within the exposed sky area, 511 keV line emission is significantly detected towards the galactic bulge region and, at a very low level, from the galactic disk. The bulge emission is highly symmetric and is centred on the galactic centre with an extension of $\sim 8^\circ$ (FWHM). The emission is equally well described by models that represent the stellar bulge or halo populations. The detection significance of the bulge emission is $\sim 50\sigma$, that of the galactic disk is $\sim 4\sigma$. The disk morphology is only weakly constrained by the present data, being compatible with both the distribution of young and old stellar populations. The 511 keV line flux from the bulge and disk components is $(1.05 \pm 0.06) \times 10^{-3}$ ph cm^{-2}s^{-1} and $(0.7 \pm 0.4) \times 10^{-3}$ ph cm^{-2}s^{-1}, respectively, corresponding to a bulge-to-disk flux ratio in the range $1-3$. Assuming a positronium fraction of $f_{\rm p} = 0.93$ this translates into annihilation rates of $(1.5 \pm 0.1) \times 10^{43}$ s^{-1} and $(0.3 \pm 0.2) \times 10^{43}$ s^{-1}, respectively. The ratio of the bulge luminosity to that of the disk is in the range $3-9$. We find no evidence for a point-like source in addition to the diffuse emission, down to a typical flux limit of $\sim 10^{-4}$ ph cm^{-2}s^{-1}. We also find no evidence for the positive latitude enhancement that has been reported from OSSE measurements; our 3σ upper flux limit for this feature is 1.5×10^{-4} ph cm^{-2}s^{-1}. The disk emission can be attributed to the β^+-decay of the radioactive species ^{26}Al and ^{44}Ti. The bulge emission arises from a different source which has only a weak or no disk component. We suggest that Type Ia supernovae and/or low-mass X-ray binaries are the prime candidates for the source of the galactic bulge positrons. Light dark matter annihilation could also explain the observed 511 keV bulge emission characteristics.

Key words. gamma rays: observations – line: profiles – Galaxy: centre

1. Introduction

Since the first detection (Johnson & Haymes 1973) and the subsequent firm identification (Leventhal et al. 1978) of the galactic 511 keV annihilation line, the origin of galactic positrons has been a lively topic of scientific debate. Among the proposed candidates for sources of positrons figure cosmic-ray interactions with the interstellar medium (Ramaty et al. 1970), pulsars (Sturrock 1971), compact objects housing either neutron stars or black holes (Ramaty & Lingenfelter 1979), gamma-ray bursts (Lingenfelter & Hueter 1984), (light) dark matter (Rudaz & Stecker 1988; Boehm et al. 2004), and stars expelling radioactive nuclei produced by nucleosynthesis, such as supernovae (Clayton 1973), hypernovae (Cassé et al. 2004), novae (Clayton & Hoyle 1974), red giants (Norgaard 1980), and Wolf-Rayet stars (Dearborn & Blake 1985). It seems difficult to disentangle the primary galactic positron source based only on theoretical grounds, mainly due to the (highly) uncertain positron yields, but also due

Send offprint requests to: Jürgen Knödlseder, e-mail : knodlseder@cesr.fr

⋆ Based on observations with INTEGRAL, an ESA project with instruments and science data centre funded by ESA member states (especially the PI countries: Denmark, France, Germany, Italy, Switzerland, Spain), Czech Republic and Poland, and with the participation of Russia and the USA.

to the uncertain distribution and duty cycle of the source populations.

Help is expected from a detailed study of the 511 keV line emission morphology. The celestial 511 keV intensity distribution should be tied to the spatial source distribution, although positron diffusion and effects associated with the annihilation physics may to some extent blur this link. First estimations of the 511 keV emission morphology were obtained by the Oriented Scintillation Spectrometer Experiment (OSSE) on-board the Compton Gamma-Ray Observatory (CGRO) satellite (Purcell et al. 1994; Cheng et al. 1997; Purcell et al. 1997; Milne et al. 2000; Milne et al. 2001), but observations were restricted to the inner Galaxy, giving only a limited view of the 511 keV emission distribution. With the launch of ESA's INTEGRAL satellite in October 2002, a new gamma-ray observatory is available that allows a detailed study of positron annihilation signatures. In particular, the imaging spectrometer SPI (Vedrenne et al. 2003), one of the two prime instruments on-board INTEGRAL, has been optimised for the study of line radiation, combining high-resolution spectroscopy (R $\sim$ 250 at 511 keV) with modest angular resolution (3° FWHM).

We present in this work an all-sky map of 511 keV gamma-ray line emission, with the goals of determining the morphology of the emission in the Galaxy and of searching for previously unknown sources of 511 keV emission anywhere in the sky. The present public data archive does not yet cover the entire celestial sphere, but the unexposed regions are limited to a few areas at high galactic latitudes, comprising less than 5% of the sky.The resulting point-source sensitivity is better than 2×10^{-4} ph cm^{-2}s^{-1} for many regions along the galactic plane, allowing for the first time the extraction of information about the distribution of positron annihilation all over the Galaxy. We do not address the distribution of positronium continuum emission in this paper, since the subtraction of the diffuse galactic continuum emission is a distinct data analysis challenge. A map of positronium continuum emission will be presented elsewhere (Weidenspointner et al., in preparation).

Earlier results on the 511 keV line emission morphology as observed by SPI have been presented by Jean et al. (2003a), Knödlseder et al. (2004a), and Weidenspointner et al. (2004), and were based on observations performed during the galactic centre deep exposure (GCDE) of 2003. Using a "light bucket" approach which neglects the coding properties of the SPI mask, Teegarden et al. (2005) derived upper limits on electron-positron annihilation radiation from the galactic disk using core-programme data combined with open-programme observations at low galactic latitudes ($|b| \leq 20°$). In the present paper we provide for the first time an all-sky analysis using all public data of the first INTEGRAL mission year.

Spectroscopic characteristics of the 511 keV line based on SPI data have been published by Jean et al. (2003a), Lonjou et al. (2004), and Churazov et al. (2005). We will present the 511 keV line profile that we obtain from the all-sky dataset elsewhere (Jean et al., in preparation).

This paper is organised as follows. Section 2 describes the observations and the data preparation. Section 3 explains the treatment of the instrumental background. In section 4, we present the first all-sky map of 511 keV gamma-ray line radiation and determine the morphology of the emission. Section 4 also describe searches for correlations with tracers of galactic source populations in order to shed light on the origin of the positrons. In section 5 we discuss the implications of the observations for the galactic origin of positrons, and we conclude in section 6.

2. Observations and Data Preparation

The data that were analysed in this work consist of those included in the December 10, 2004 public INTEGRAL data release (i.e. orbital revolutions 19-76, 79-80, 89-122) plus the INTEGRAL Science Working Team data of the Vela region observed during revolutions 81-88. The data span the IJD epoch $1073.394 - 1383.573$, where IJD is the Julian Date minus 2 451 544.5 days.

We screened the data for anomalously high counting rates (typically occurring at the beginning and the end of an orbital revolution due to the exit and entry of the radiation belts) and for periods of solar activity (as monitored by the SPI anticoincidence system) and excluded these periods from the data. This data screening has turned out to be crucial for reducing the systematic uncertainties in the data analysis related to instrumental background variations. After data screening, the dataset consists of 6821 pointed observations, with a total exposure time of 15.3 Ms. Typical exposure times per pointing are $1200 - 3400$ seconds, but a few long staring observations of up to 113 ks exposure time are also included.

Figure 1 shows a map of the resulting effective SPI exposure at 511 keV. The maximum exposure of 2.1×10^8 cm^2 s occurs towards the galactic centre region thanks to data obtained during a long dedicated observation of this region.[1] A relatively uniform exposure of $\sim 3 \times 10^7$ cm^2 s has been achieved for galactic longitudes $|l| \leq 50°$ and latitudes $|b| \leq 15°$. Regions of peculiarly high exposure ($\sim 5 \times 10^7$ cm^2 s) are found in Cygnus, Vela and towards the Large Magellanic Cloud. In addition, particularly well exposed sources ($\gtrsim 2 \times 10^7$ cm^2 s) are the Crab nebula, 3C 273, NGC 4151, M 94, NGC 936 (during the SN2003 gs outburst) and the Coma cluster. Unexposed regions are found mostly at intermediate galactic latitudes ($|b| \sim 30° - 60°$), and towards the south galactic pole.

A map of the resulting narrow-line 3σ point-source sensitivity of SPI at 511 keV is shown in Fig. 2. To evaluate the sensitivity, an energy band of 7 keV centred at 511 keV has been used. The choice of such a relatively wide band eliminates any bias due to the germanium detector degradation and annealing cycles, as well as any bias/effect due

[1] To obtain the effective exposure time, the exposure has to be divided by the effective area at 511 keV of about 75 cm^2.

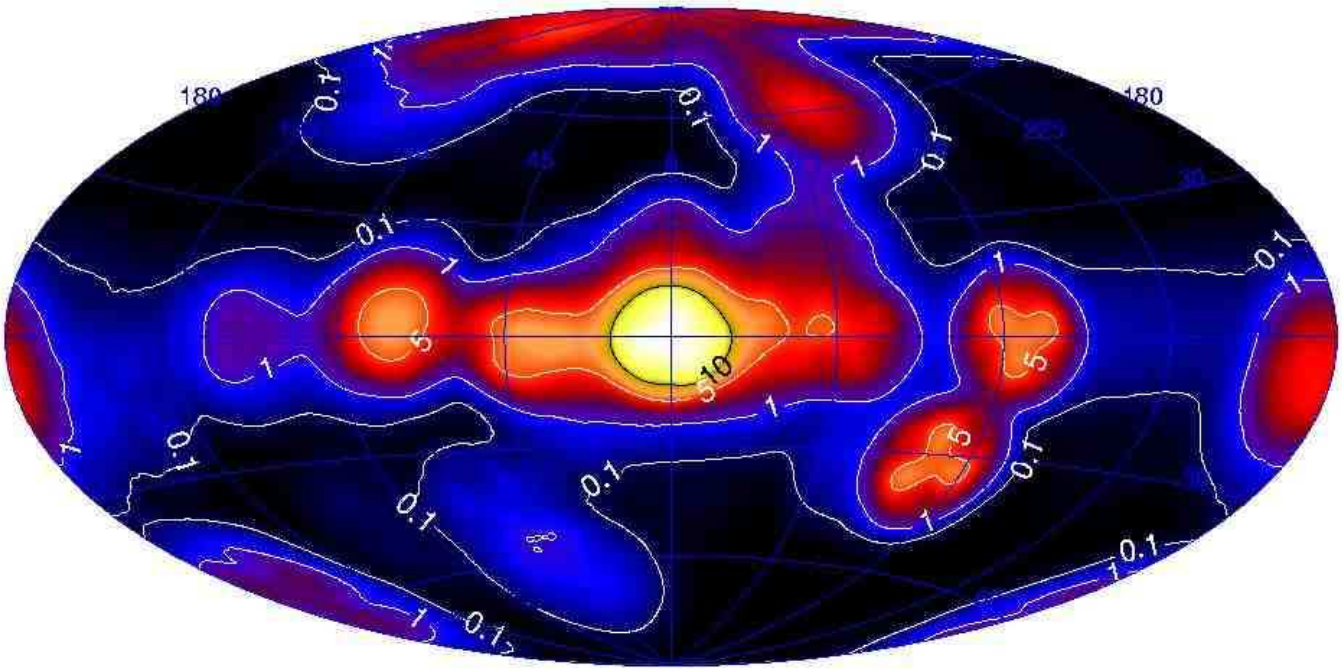

Fig. 1. Map of the effective SPI exposure at 511 keV for the dataset analysed in this work. The contours are labelled in units of 10^7 cm^2 s, corresponding to 13 ks (0.1), 133 ks (1), 667 ks (5), and 1.3 Ms (10) of effective exposure times.

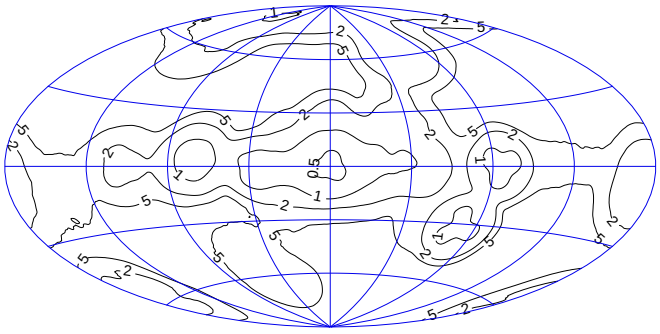

Fig. 2. SPI narrow line 3σ point-source sensitivity at 511 keV for the analysis interval $507.5 - 514.5$ keV (contours are labelled in units of 10^{-4} ph cm^{-2}s^{-1}).

to gain calibration uncertainties. It also takes into account moderate 511 keV line broadening, as reported by Jean et al. (2003a).

Over large regions of the sky, and in particular in the galactic plane, a sensitivity better than 2×10^{-4} ph cm^{-2}s^{-1} is reached. A best point-source sensitivity of 5×10^{-5} ph cm^{-2}s^{-1} is achieved towards the galactic centre direction. The sensitivity to extended diffuse emission becomes slightly worse with increasing emission size, and depends on the exposure pattern in the region of interest. For example, for a 2d angular Gaussian surface brightness distribution centred on the galactic centre, the 511 keV line sensitivity worsens from 5×10^{-5} ph cm^{-2}s^{-1} for a galactic centre point-source to 7×10^{-5} ph cm^{-2}s^{-1} for an extended source of 8° FWHM.

Only single-detector event data have been analysed in this work (multiple-detector event data do not contribute significantly to the SPI sensitivity at an energy of 511 keV; c.f. Roques et al. 2003). Energy calibration was performed orbit-wise, resulting in a relative (orbit-to-orbit) calibration precision of ~ 0.01 keV and an absolute accuracy of ~ 0.05 keV (Lonjou et al. 2004).

The data have been analysed by sorting the events in a 3-dimensional data-space, spanned by the (calibrated) event energy, the detector number, and the SPI pointing number. An energy binning of 0.5 keV has been chosen, well below the instrumental energy resolution of 2.12 keV at 511 keV.

3. Background modelling

The most crucial step in SPI data analysis consists of the precise modelling of the time variability of the instrumental background. In the region of the 511 keV line, the instrumental background consists of a nearly flat continuum and a (broadened) instrumental 511 keV line originating from positron annihilation within the telescope (Teegarden et al. 2004). Since the time variation of the continuum component differs from that of the line component we model them independently. The background model for a given data-space bin, indexed in the following by the pointing number p, the detector number d and the energy bin e, is then given by

$$b_{p,d,e} = b^{\rm cont}_{p,d,e} + b^{\rm line}_{p,d,e} \quad (1)$$

(note that for the analysis presented in this work a single energy bin has been used, covering the energy interval

$507.5 - 514.5$ keV; however, for clarity and reference in future works we give here the complete energy-dependent formalism).

The time variation of the continuum component is extrapolated from that observed in an continuum energy band adjacent to the 511 keV line. We used the energy band $E_{\rm adj} = 523 - 545$ keV, situated above the 511 keV line, in order to exclude any bias due to positronium continuum emission that appears below 511 keV. To reduce the statistical uncertainty that arises from the limited counting statistics, we smoothed the time variation by locally adjusting the rate of saturated events in the germanium detectors (GEDSAT) to the adjacent counting rate (GEDSAT turned out to provide a good first order tracer of the background variation in SPI; c.f. Jean et al. 2003b). The predicted number of continuum background counts in data-space bin (p, d, e) is then given by

$$b^{\rm cont}_{p,d,e} = g_{p,d} \times T_{p,d} \times \frac{\Delta_e}{\sum_{e' \in E_{\rm adj}} \Delta_{e'}} \times \frac{\sum_{p'=p-\Delta_p}^{p+\Delta_p} \sum_{e' \in E_{\rm adj}} n_{p',d,e'}}{\sum_{p'=p-\Delta_p}^{p+\Delta_p} g_{p',d} \times T_{p',d}}, \quad (2)$$

where

- $g_{p,d}$ is the GEDSAT rate for detector d, averaged over the time period spanned by pointing p, given in units of counts $\rm s^{-1}$,
- $T_{p',d}$ is the lifetime for detector d during pointing p', given in units of seconds,
- Δ_e is the energy bin size for spectral bin e, given in units of keV (here $\Delta_e = 0.5$ keV), and
- $n_{p',d,e'}$ is the number of observed counts for pointing p', detector d, and energy bin e', given in units of counts.

The number of pointings used for smoothing, given by $2\Delta_p + 1$, is determined for each pointing p and detector d by satisfying the constraint

$$\min_{\Delta_p \geq 0} \left(\sum_{p'=p-\Delta_p}^{p+\Delta_p} T_{p',d} \geq T_{\rm min} \right). \quad (3)$$

An accumulated lifetime of $T_{\rm min} = 20$ hours has shown to provide an optimum compromise between reducing the statistical uncertainty (due to the limited number of events in the adjacent energy band) and reducing the systematic uncertainty (due to the fact that the GEDSAT rate does not predict the background to infinite precision). In other words, continuum background variations shorter than ~ 20 hours are modelled by the GEDSAT rate while variations on longer time scales are modelled by the observed event rate in the $523 - 545$ keV band.

The time variation of the line component was modelled for each detector d and energy bin e separately using a multi-component template of the form

$$b^{\rm line}_{p,d,e} = \beta^{(1)}_{d,e} + \beta^{(2)}_{d,e} \times g_{p,d} + \beta^{(3)}_{d,e} \int_{t_0}^{t} g_d(t') e^{(t'-t)/\tau} {\rm d}t'. \quad (4)$$

This template consists of a constant term $\beta^{(1)}_{d,e}$ plus the GEDSAT rate $g_{p,d}$ scaled by $\beta^{(2)}_{d,e}$ plus the GEDSAT rate $g_d(t')$ convolved with an exponential decay law, scaled by $\beta^{(3)}_{d,e}$ (the convolution integral is taken from the start of the INTEGRAL mission t_0 up to date t). The coefficients $\beta^{(i)}_{d,e}$ of the template are adjusted during the analysis for each SPI detector d and energy bin e using a maximum likelihood fitting procedure (again, in the analysis presented in this paper only a single energy bin is used). The constant term has been introduced to provide for non-linearities between the background variation and the GEDSAT rate. In fact, it turns out that $\beta^{(1)}_{d,e}$ are negative. An equally good background predictor is obtained if the GEDSAT rate raised to a power of ~ 1.1 is taken, but using a constant instead of a powerlaw has the advantage of having the background variation template decomposed into a linear combination of terms. The third component makes provision for a long term build-up that is seen in the intensity of the 511 keV background line, and that is tentatively attributed to production of the isotope ^{65}Zn which has a decay time of $\tau = 352$ days. The precise value of τ is in fact weakly constrained by the present data, and a linear slope provides an equally good fit of the instrumental 511 keV line background.

Although the background model defined by Eqs. (1)–(4), which hereafter is called model `DETE`, predicts the instrumental background to good accuracy, significant residuals remain after subtracting off the background model and a model of the sky intensity distribution from the data (c.f. Fig. 3). We found that these residuals can lead to systematic biases in the study of the morphology of the 511 keV emission, in particular for the determination of the longitude profile of the emission. These biases can be explained by the telescope pointing strategy that has been adopted for a large fraction of the galactic centre deep exposure (GCDE) of the INTEGRAL core program: a slow (5°/day) scan of the galactic plane from negative towards positive longitudes combined with rapid (3°/hour) excursions in galactic latitude. As result, the longitude profile of the 511 keV line emission is encoded in count rate variations on timescales of days while the latitude profile is encoded in count rate variations on timescales of hours. Within a few hours the SPI instrumental background is sufficiently stable to be accurately predicted by our model, hence the latitude profile is rather well determined. However, on timescales of days the background variations are more difficult to predict to sufficient accuracy, potentially leading to systematic trends in the determination of the longitude profile.[2]

[2] In a preliminary analysis in which we treated a much smaller dataset, systematic background uncertainties suggested a significant elongation of the galactic centre bulge emission along the galactic plane. This elongation was artificial and had been produced by background variations that were not fully explained by our model. Removing the short period of data with the strongest background variations removed also the apparent elongation of the bulge emission.

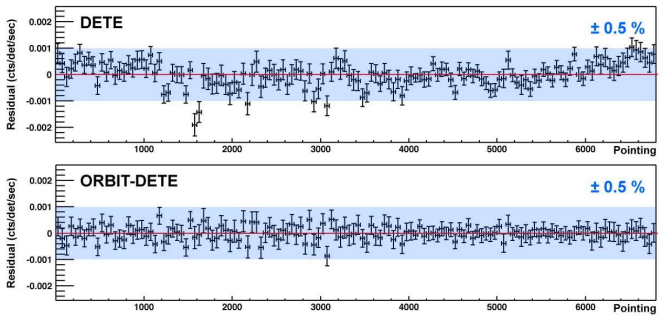

Fig. 3. Residual count rate as function of pointing number for the DETE (top) and ORBIT-DETE (bottom) background models for the energy band 507.5 − 514.5 keV. In addition to the background models the best fitting 2d Gaussian surface brightness model (c.f. section 4.2.2) has been subtracted from the data. For clarity, the data have been rebinned into groups of 50 pointings. The shaded area indicates count rate variations of ±0.5%. For comparison, the maximum 511 keV line signal amplitude corresponds to approximately ∼ 2% of the observed count rate.

In order to improve the background model on long timescales, we studied also a class of models where we adjust the longterm variations during model fitting. For this purpose we adjust the model parameters $\beta_{d,e}^{(2)}$ not only for all SPI detectors but also for time intervals of fixed duration T. In this way, systematic uncertainties in the background model on timescales longer than T are removed. Fitting the background for each orbital revolution ($T \sim 3$ days) is adequate to reduce systematic trends well below the statistical uncertainties (c.f. bottom panel of Fig. 3). This method is similar to the method that we applied in our earlier works (Jean et al. 2003a; Knödlseder et al. 2004a; Weidenspointner et al. 2004), with the difference that we now also fit the background model for each of the SPI detectors separately, and that we included in addition a constant term and a build-up term in the model (see Eq. 4). Hereafter this second background model is called ORBIT-DETE.

The introduction of additional parameters in ORBIT-DETE with respect to DETE leads to a substantial loss in sensitivity. The detection significance of galactic centre 511 keV line emission drops from $\sim 50\sigma$ for DETE to $\sim 22\sigma$ for ORBIT-DETE. However, it was found that the statistical accuracy of the morphology determination, which is driven by the count rate contrast in the data-space rather than the count rate level, is not degraded by the introduction of additional parameters, as long as $T \gtrsim 2$ days. Consequently, using the ORBIT-DETE model for the morphological characterisation of the 511 keV line emission is the optimum choice that keeps a high statistical accuracy while reducing the systematic uncertainties in the analysis.

On the other hand, despite the systematic uncertainties, DETE is accurate enough to allow for a precise determination of 511 keV line flux levels. This is related to the fact that flux measurements require an average determination of the count rate level and are not sensitive to the count rate contrast. Apparently, the count rate residuals approximately average to zero (c.f. Fig. 3).

We therefore opted for a two step approach where we first determine the morphology using ORBIT-DETE, and then, using the optimum morphology parameters, determine the 511 keV flux using DETE. In this way we recover the good sensitivity of SPI for 511 keV flux measurements that was reduced by a factor of ~ 2 by the usage of ORBIT-DETE. The comparison of the flux levels determined using DETE and ORBIT-DETE provides us with a measure of the systematic uncertainty in the flux determination, which in general is smaller than the statistical uncertainty obtained with DETE. We add the systematic to the statistical uncertainty in quadrature and quote the result as total error on the flux measurement. In cases where uncertainties in the morphology (such as the size of the emission region) introduce some uncertainty on the flux, we have also added this uncertainty to the total error in quadrature.

4. Results

4.1. Imaging

To determine a model independent map of the 511 keV gamma-ray line intensity distribution over the sky, we employed the Richardson-Lucy algorithm (Richardson 1972; Lucy 1974). This type of algorithm is widely used for image deconvolution, and has in particular been successfully employed for the analysis of gamma-ray data of CGRO (Knödlseder et al. 1999a; Milne et al. 2000).

We implemented the accelerated version ML-LINB-1 of Kaufman (1987) of the Richardson-Lucy algorithm for our analysis, which iteratively updates the sky intensity distribution $f_j^k \rightarrow f_j^{k+1}$ using the relation

$$f_j^{k+1} = f_j^k + \lambda^k w_j f_j^k \left(\frac{\sum_{i=1}^{N} \left(\frac{n_i}{e_i^k} - 1 \right) R_{ij}}{\sum_{i=1}^{N} R_{ij}} \right) \quad (5)$$

where R_{ij} is the instrumental response matrix (linking the data space, indexed by i, to the image space, indexed by j), n_i is the number of counts measured in data space bin i, $e_i^k = \sum_{j=1}^{M} R_{ij} f_j^k + b_i$ is the predicted number of counts in data space bin i after iteration k (b_i being the predicted number of instrumental background counts for bin i), N and M are the dimensions of the data and image space, respectively, and λ^k is an acceleration factor that is obtained by constrained maximum likelihood fitting (with the constraint that the resulting sky intensities remain positive).

To avoid noise artefacts in the weakly exposed regions of the sky, we weighted the image increment with a quantity that is related to the sensitivity of the instrument, given by $w_j = (\sum_{i=1}^{N} R_{ij})^{1/2}$. We verified that introducing this weighting had no impact on the image reconstruction in the well exposed regions of the sky. In addition, we

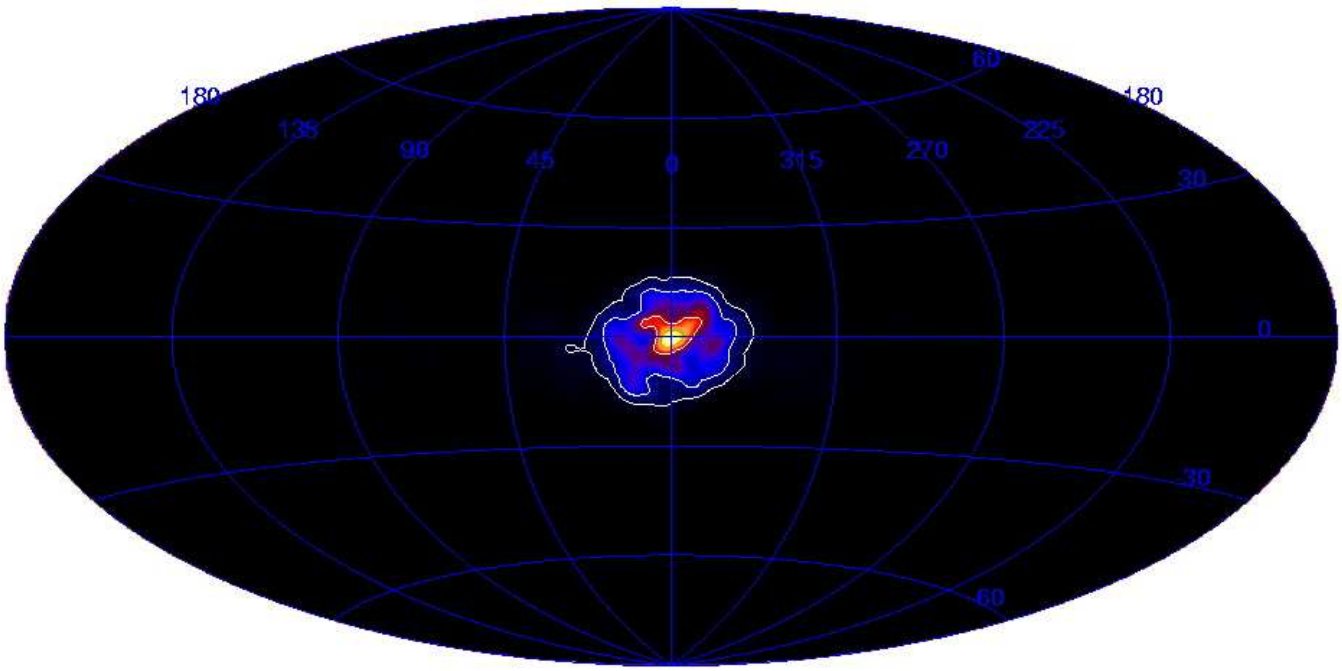

Fig. 4. Richardson-Lucy image of 511 keV gamma-ray line emission (iteration 17). Contour levels indicate intensity levels of 10^{-2}, 10^{-3}, and 10^{-4} ph cm^{-2}s^{-1}sr^{-1} (from the centre outwards).

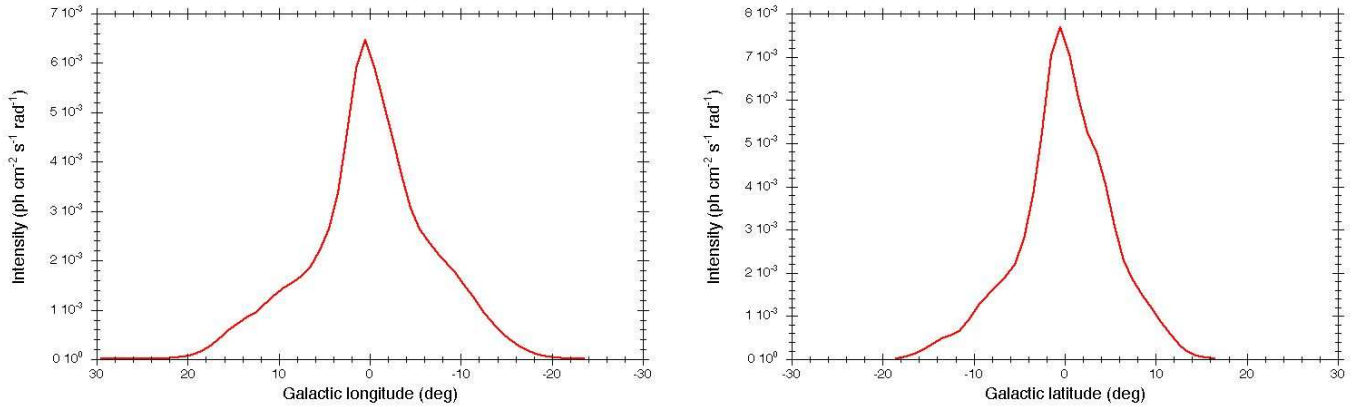

Fig. 5. Longitude and latitude profiles of the image shown in Fig. 4 (integration range $|l| \leq 30°$, $|b| \leq 30°$).

smoothed the iterative corrections on the right hand side of Eq. 5 using a $5° \times 5°$ boxcar average. In this way the effective number of free parameters in the reconstruction is reduced and image noise is damped to an acceptable level. The application of more sophisticated image reconstruction methods involving wavelet based multi-resolution algorithms aiming at a complete suppression of image noise (Knödlseder et al. 1999a) will be presented elsewhere.

The resulting all-sky image of the 511 keV line emission is shown in Fig. 4, longitude and latitude profiles of the emission are shown in Fig. 5. We have chosen to stop the iterative procedure after iteration 17 since at this point the recovered flux and the fit quality correspond approximately to the values that we achieve by fitting astrophysical models to the data (c.f. section 4.2). In this way we make sure that we are not in the regime of overfitting, which is characterised by substantial image noise and artificial image structures. On the other hand, simulations showed that faint diffuse emission, as expected for example for a galactic disk component, would not be recovered at this point.

Figure 4 reveals that the 511 keV sky is dominated by prominent emission from the bulge region of the Galaxy. Beyond the galactic bulge, no additional 511 keV emission is seen all over the sky, despite the good exposure in some regions (e.g. Cygnus, Vela, LMC, anticentre, north galactic pole region). The 511 keV emission appears symmetric and centred on the galactic centre, with indications for a slight latitude flattening. The latitude flattening could be either due to an inherent asymmetry of the bulge component or due to the presence of an underlying faint galactic disk component. Indeed, if the Richardson-Lucy iterations are continued, a faint disk-like structure emerges (c.f. Fig. 6). Yet the image starts to become pol-

luted by noise and we cannot exclude the possibility that the apparent disk emission is artificially created by the exposure pattern that follows the galactic plane. Therefore we employ more quantitative methods in the next section to assess the significance of the possible disk emission.

By fitting Gaussian functions to the longitude and latitude profiles of the image (c.f. Fig. 5) we estimate the extent of the emission to $\sim 13^\circ \times 10^\circ$ (FWHM). Figure 5 indicates, however, that the emission profiles are not well represented by Gaussian functions. The emission is better described by a compact (FWHM $\sim 5^\circ$) core and a more extended halo (FWHM $10^\circ - 20^\circ$). We want to emphasise, however, that this qualitative analysis should not be pushed too far, since image deconvolution is a non-linear process which is easily affected by image noise and exposure biases.

4.2. Morphological characterisation

4.2.1. Method

To make a quantitative assessment of the morphology of the 511 keV line emission we use a maximum likelihood multi-component model fitting algorithm. Assuming Poisson noise for the measured number n_i of events in each of the N data-space bins, the algorithm maximises the log likelihood

$$\ln L = \sum_{i=1}^{N} n_i \ln e_i - e_i - \ln n_i!, \qquad (6)$$

where $e_i = \sum_k \alpha_k s_i^k + b_i(\boldsymbol{\beta})$ is the predicted number of (source plus background) counts in data space bin i, $s_i^k = \sum_{j=1}^{M} f_j^k R_{ij}$ is the sky intensity model f_j^k folded into the data space (R_{ij} being the instrumental response matrix), $b_i(\boldsymbol{\beta})$ is the background model (c.f. Fig. 1), and α_k and $\boldsymbol{\beta}$ are scaling factors for the sky intensity and the background model, respectively, that are adjusted by the fit.

Detection significances (and parameter errors) are estimated using the maximum likelihood ratio test (Cash 1979). We calculate the maximum log likelihood-ratio MLR $= -2(\ln L_0 - \ln L_1)$ between two models (hypotheses), where for the first one we constrain a number p of the parameters to specific values (resulting in L_0) while for the second one all parameters are left free (resulting in L_1). In the case that L_1 provides a satisfactory fit of the data, MLR is then distributed like a χ^2_p distribution with p degrees of freedom. Statistical parameter errors were estimated using the formalism of Strong (1985). Throughout this paper the error bars quoted are 1σ.

We call the maximum log likelihood-ratio (MLR) of a model the difference between the log likelihood obtained by fitting all model parameters and the log likelihood obtained by fitting only the background model to the data (i.e. for L_1 all parameters α_k and $\boldsymbol{\beta}$ vary freely while for L_0 all α_k are constrained to zero and only the $\boldsymbol{\beta}$ are allowed to vary). To compare models with different numbers of free parameters, we quote the reduced maximum log likelihood-ratio, RMLR = MLR − DOF, with DOF being the number of free parameters α_k of the sky intensity model.

Table 1. Morphology of the emission assuming a 2d angular Gaussian surface brightness distribution.

Quantity	Measured Value
RMLR (DOF)	462.2 (5)
l_0	$-0.6^\circ \pm 0.3^\circ$
b_0	$+0.1^\circ \pm 0.3^\circ$
Δl (FWHM)	$8.1^\circ \pm 0.9^\circ$
Δb (FWHM)	$7.2^\circ \pm 0.9^\circ$
511 keV flux (10^{-3} ph cm^{-2}s^{-1})	1.09 ± 0.04

4.2.2. 2d surface brightness distribution

As a first step we characterise the apparent morphology of the 511 keV line emission on the sky using a 2d angular Gaussian surface brightness distribution for which we determined the centroid, l_0, b_0, the longitude and latitude extent, $\Delta l, \Delta b$, and the 511 keV line flux. The results of this analysis are summarised in Table 1, the best fitting model intensity distribution is shown in Fig. 8.

The analysis confirms our earlier findings (Jean et al. 2003a; Knödlseder et al. 2004a; Weidenspointner et al. 2004) of a compact and symmetric 511 keV line emission distribution towards the galactic centre. The centroid of the emission appears slightly offset from the galactic centre direction, at the statistical 2σ level, but we do not claim that this offset is significant. From our earlier analyses we learned that the centroid can be shifted by this amount simply from the combined effect of statistical and systematic biases in the modelling of the instrumental background.

Within the statistical uncertainties, the emission appears fully symmetric, with an extension of $\sim 8^\circ$ (FWHM). Formally, we determine a marginal emission flattening of $\Delta b/\Delta l = 0.89 \pm 0.14$. The total 511 keV flux is $(1.09 \pm 0.04) \times 10^{-3}$ ph cm^{-2}s^{-1}, where the quoted error includes the uncertainty in the extent of the emission and the statistical and systematic measurement errors (c.f. section 2).

The RMLR of 462.2 that has been obtained using the `ORBIT-DETE` background model converts into a formal detection significance of 22σ. Using the `DETE` background model and including the systematic uncertainties results in a substantially higher detection significance of 34σ. Neglecting systematic uncertainties would even boost the detection significance towards 49σ.

4.2.3. Galactic models

To determine the galactic positron-electron annihilation rate requires modelling the spatial distribution of the

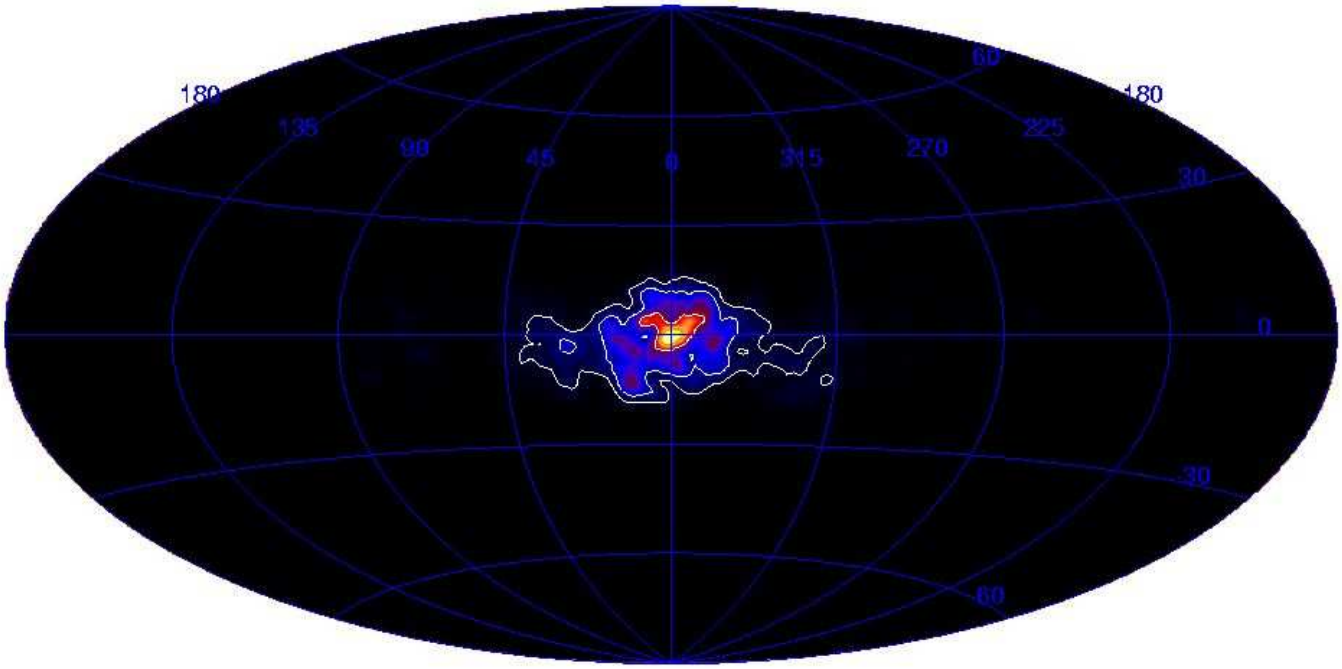

Fig. 6. Richardson-Lucy image after iteration 25. Contour levels are similar to Fig. 4.

positron-electron annihilation. The 511 keV photon luminosity L_{511} is related to the positron luminosity L_p through $L_{511} = (2 - 1.5 f_p) \times L_p$ where f_p is the positronium (Ps) fraction, defined as the fraction of positrons that decay via positronium formation (Brown, & Leventhal 1987). Using $f_p = 0.93 \pm 0.04$ that has been determined from OSSE observations (Kinzer et al. 2001) results in a conversion from 511 keV photon luminosity to a positron-electron annihilation rate of $L_p = (1.64 \pm 0.06) \times L_{511}$.

We here compare models of bulge, disk, and halo components with the data. Based on galactic model density distributions $\rho(x, y, z)$ we calculate the expected all-sky 511 keV intensity $f(l, b)$ towards direction (l, b) by integrating the volume emissivity $\rho(x, y, z)$ along the line of sight s:

$$f(l,b) = \frac{1}{4\pi} \int \rho(x,y,z) \mathrm{d}s \tag{7}$$

(the galactic centre has been assumed to be at a distance of $R_\odot = 8.5$ kpc). Galactic 511 keV photon luminosities are calculated by integrating $\rho(x, y, z)$ over the galactic volume,

$$L_p = \int \rho(x,y,z) s^2 \mathrm{d}s \mathrm{d}\Omega \tag{8}$$

assuming an outer Galaxy radius of $R_{\max} = 15$ kpc.

Since the 511 keV line emission is primarily arising from the galactic centre region we fitted in a first step models of the galactic stellar bulge to the data. To account for uncertainties in our knowledge about the morphology of this component (which are related to our location in the galactic plane amid the obscuration by interstellar dust) we compared a variety of proposed bulge models to the data. The models were gathered from Dwek et al. (1995) and Freudenreich (1998), who modelled the distribution of K and M giant stars using DIRBE near-infrared skymaps, and from Picaud & Robin (2004) who analysed data from the DENIS near-infrared survey. There is an accumulating body of evidence that the stellar distribution in the bulge is bar-shaped, and except for models G0 and E0, all employed bulge models have triaxial morphologies that differ in the orientation angles, the scale lengths, and the radial density profiles. Details of the models are given in Appendix A, the results of the analysis are summarised in Table 2, and best fitting 511 keV intensity distributions are shown in Fig. 8.

The best fitting bulge models are E3, G3, S_F, and E_F. Reasonably good fits are also obtained for P_F and S_{PR}, while only moderate fits are achieved for the remaining models. Our ranking is similar to that established from the analysis of the DIRBE and DENIS near-infrared data (Dwek et al. 1995; Freudenreich 1998; Picaud & Robin 2004). The best fitting bulge models fit the data as well as the adjusted 2d angular Gaussian surface brightness distribution. This means that models of the galactic stellar bulge are able to explain satisfactorily the morphology of the 511 keV bulge emission.

In a second step we fitted the 511 keV emission using parametric models of the galactic bulge and halo morphology in order to determine the scale of the emission. For the bulge models G0' and E0' we adjust the radial scale length (R_0) and vertical scale height (z_0), while for the galactic halo model H' we determine the density slope powerlaw index (n), the inner cutoff radius (a_c), and the axis ratio (ϵ). In addition, we employed a model composed of a set of galactocentric nested shells of constant density

Table 2. Galaxy model fitting results (see text). The columns give (1) the model, (2) the RMLR (obtained using the `ORBIT-DETE` background model) and the number of free model parameters (DOF), (3) the bulge scale length, (4) the bulge scale height, (5)-(8) the 511 keV photon luminosity of the model components, and (9)-(12) the total 4π integrated 511 keV line all-sky flux in each of the model components. The prime indicates model components for which the scaling parameters were adjusted by the fit. The figures in parenthesis quoted in columns (5)-(12) indicate 1σ uncertainties in the last digit.

Model	RMLR (DOF)	R_0 (kpc)	z_0 (kpc)	L_{511} (10^{43} ph s^{-1})				511 keV line flux (10^{-3} ph cm^{-2}s^{-1})			
				bulge	disk	halo	total	bulge	disk	halo	total
G0	447.5 (1)	0.91	0.51	1.04(3)			1.04(3)	1.22(4)			1.22(4)
G1	445.7 (1)			0.97(3)			0.97(3)	1.19(4)			1.19(4)
G2	450.8 (1)			0.98(3)			0.98(3)	1.18(3)			1.18(3)
G3	462.2 (1)			0.98(3)			0.98(3)	1.18(3)			1.18(3)
E1	441.8 (1)			0.99(4)			0.99(4)	1.19(4)			1.19(4)
E2	453.1 (1)			1.01(3)			1.01(3)	1.19(3)			1.19(3)
E3	464.9 (1)			1.00(3)			1.00(3)	1.17(3)			1.17(3)
S_F	459.0 (1)			0.96(3)			0.96(3)	1.19(3)			1.19(3)
E_F	459.0 (1)			0.93(2)			0.93(2)	1.19(3)			1.19(3)
P_F	456.5 (1)			0.94(3)			0.94(3)	1.16(3)			1.16(3)
S_{PR}	456.3 (1)			0.94(2)			0.94(2)	1.22(3)			1.22(3)
G0'	462.5 (3)	0.52(6)	0.45(5)	0.94(4)			0.94(4)	1.09(4)			1.09(4)
E0'	464.2 (3)	0.37(5)	0.42(7)	0.98(5)			0.98(5)	1.15(5)			1.15(5)
H'	468.4 (4)					1.6(3)	1.6(3)			2.2(4)	2.2(4)
Shells	469.0 (2)			0.97(3)			0.97(3)	1.13(3)			1.13(3)
E3+D0	466.3 (2)			0.95(3)	0.11(5)		1.05(4)	1.11(4)	0.4(2)		1.53(5)
G0'+D0	465.2 (4)	0.48(6)	0.46(6)	0.87(4)	0.15(5)		1.03(5)	1.01(5)	0.6(2)		1.61(7)
E0'+D0	466.2 (4)	0.34(4)	0.44(8)	0.92(5)	0.14(5)		1.06(5)	1.07(6)	0.5(2)		1.61(8)
H'+D0	468.2 (5)				0.09(8)	1.2(3)	1.3(3)		0.4(3)	1.6(5)	2.1(5)
Shells+D0	472.2 (3)			0.91(4)	0.15(5)		1.05(4)	1.05(4)	0.6(2)		1.62(6)
E3+D1	468.8 (2)			0.93(4)	0.23(8)		1.15(6)	1.09(5)	0.8(3)		1.90(9)
G0'+D1	468.6 (4)	0.47(6)	0.45(6)	0.84(5)	0.31(9)		1.15(6)	0.98(5)	1.1(3)		2.1(1)
E0'+D1	469.5 (4)	0.33(4)	0.42(8)	0.89(5)	0.29(9)		1.17(7)	1.03(6)	1.0(3)		2.1(1)
H'+D1	470.4 (5)				0.3(1)	1.2(3)	1.4(3)		0.9(4)	1.5(4)	2.4(5)
Shells+D1	474.9 (3)			0.88(4)	0.29(8)		1.17(6)	1.03(5)	1.0(3)		2.0(1)

(model 'Shells') to determine the radial density profile of the 511 keV emission. We varied the radii of the shells and the number of shells in order to maximise the MLR, whilst limiting the number of shells to the minimum required to satisfactorily describe the data.

The data suggest a symmetric bulge emission profile, with scale lengths between 300 and 600 pc. The RMLRs are comparable to the best fitting bulge models that we tested before. The data are equally well fitted by a model of the galactic halo, with a density powerlaw index of $n = 3.0 \pm 0.3$, an inner cutoff radius of $a_c = 0.39 \pm 0.08$ kpc, and a flattening of $\epsilon = 0.81 \pm 0.12$. Most studies of the stellar halo population suggest power indices between 2.4 and 3.5 and flattenings in the range 0.6 to 1.0, while the inner cutoff radius is basically undetermined (Robin et al. 2000 and references therein). Our values are compatible with those of the stellar halo population, but the large uncertainties in the stellar halo morphology do not allow firm conclusions to be drawn.

The nested shell model provides the best fit to the data thanks to its flexibility in adjusting the radial density profile of the emission. A satisfactory fit is achieved by using two shells with radii $0-0.5$ and $0.5-1.5$ kpc; splitting up these shells in a finer binning, moving the shell interface radius or adding more shells does not significantly improve the fit. In particular, we detect no significant 511 keV bulge emission from galactocentric distances $\gtrsim 1.5$ kpc. The radial dependence of the 511 keV volume emissivity is plotted in Fig. 7. For illustration we added the result of a third shell to the figure that covers radial distances of $1.5-3.0$ kpc and for which the flux is consistent with zero. Our fit reveals a drop in the annihilation emissivity by one order of magnitude between the inner $0-0.5$ kpc and the outer $0.5-1.5$ kpc shell, confirming the existence of a narrow core plus an extended halo of 511 keV emission that has already been suggested by the imaging analysis (c.f. section 4.1).

In a third step we added galactic disk components to the bulge and halo models. For the galactic disk we tested models of young (model D0) and old (model D1) stellar populations (Robin et al. 2003). With both models we find clear evidence for 511 keV line emission from the galac-

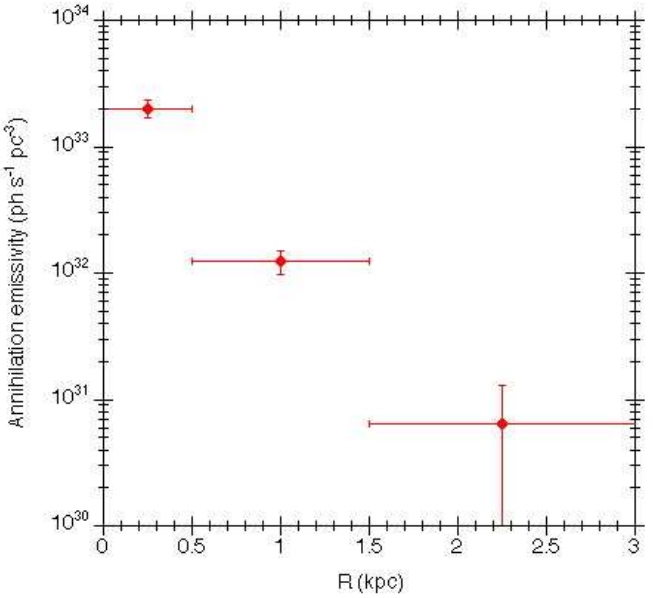

Fig. 7. Radial dependence of the 511 keV volume emissivity as derived from the bulge model 'Shells'.

Table 3. Summary of model fitting results. Fluxes are given as total 4π integrated all-sky values. Annihilation rates have been calculated assuming $f_{\rm p} = 0.93$.

Quantity	Bulge	Halo	Disk
Flux (10^{-3} ph cm^{-2}s^{-1})	1.05 ± 0.06	1.6 ± 0.5	0.7 ± 0.4
L_{511} (10^{43} ph s^{-1})	0.90 ± 0.06	1.2 ± 0.3	0.2 ± 0.1
$L_{\rm p}$ (10^{43} s^{-1})	1.50 ± 0.10	2.0 ± 0.5	0.3 ± 0.2
Total flux (10^{-3} ph cm^{-2}s^{-1})			$1.5 - 2.9$
Total L_{511} (10^{43} ph s^{-1})			$1.0 - 1.7$
Total $L_{\rm p}$ (10^{43} s^{-1})			$1.6 - 2.8$
B/D flux ratio			$1 - 3$
B/D luminosity ratio			$3 - 9$

tic disk. Adding disk models D0 and D1 to bulge or halo models consistently improves the fit leading to a detection of the disk emission at the $3-4\sigma$ level.[3] Formally, D1 provides a better fit than D0, but the difference is marginal. The signal from the disk is still too faint in our present dataset to deduce anything about its morphology.

The flux, luminosity and annihilation rate in the bulge, halo and disk components are summarised in Table 3. Recall that the bulge and halo components are alternatives and their contribution should not be added to derive the total galactic values. Either component provides an almost equally good fit to the data. Due to their degeneracy fitting both simultaneously is not meaningful.

The halo model leads to a considerably larger flux, luminosity and annihilation rate than the bulge model due to the presence of a flat and extended tail in this distribution (c.f. Fig. 8). Currently, our data do not allow to detect this tail, and thus, they do not allow to discriminate between bulge and halo models. Future deep observations at intermediate galactic latitudes that are scheduled for the INTEGRAL AO-3 observing period aim in measuring this emission tail, promising to provide constraints that will allow in the future to disentangle between the different emission morphologies.

The data suggest bulge-to-disk 511 keV flux ratios in the range $1 - 3$, where the lower boundary is obtained for the short scale-length old stellar disk model D1 which suggests larger disk flux values than the young stellar disk model D0. Halo-to-disk 511 keV flux ratios are even larger, in the range $2-4$, owing to the larger flux in the halo component. The large uncertainty in these ratios arises from the low intensity of the galactic disk component, which for the analysed dataset is just above the SPI detection limit.

We also note that the bulge-to-disk 511 keV photon luminosity ratio is much higher than the bulge-to-disk flux ratio and lies in the range $3 - 9$. This difference is explained by the fact that the average squared distance $\bar{s}^2 = \int \rho(s) s^2 {\rm d}s{\rm d}\Omega / \int \rho(s) {\rm d}s{\rm d}\Omega$, which defines the distance at which a source of luminosity $L_{\rm p}$ produces the observed 511 keV line flux, is smaller for the galactic disk than for the galactic bulge. In other words, to produce the same 511 keV flux at Earth, the intrinsic luminosity of the bulge has to be larger than that of the disk.[4] It is therefore important to quote explicitly the quantity for which we discuss the bulge-to-disk ratio. The same rational also holds for the halo-to-disk 511 keV photon luminosity ratio, which is larger than the corresponding flux ratio, and which is comprised between $4 - 13$.

4.3. Correlation with tracer maps

To gain insight into the nature of the galactic positron sources, we searched for correlations between the 511 keV line emission morphology and all-sky intensity distributions observed at other wavelengths. This work was inspired by a similar study that Knödlseder et al. (1999b) performed to understand the morphology of the 1.8 MeV gamma-ray line emission (arising from radioactive decay of ^{26}Al) observed by the COMPTEL telescope aboard CGRO. Through their analysis, the authors could establish a tight correlation between the morphology of galactic microwave free-free emission and that of 1.8 MeV line emission, hinting towards a massive star origin of ^{26}Al.

[3] Using the quoted RMLRs, the formal significance of the disk emission amounts only to $2 - 3\sigma$. However, the tabulated RMLRs have been obtained using the `ORBIT-DETE` background model which is less sensitive to 511 keV line emission than the `DETE` model. Using the procedure outlined in section 3 we reduce the flux uncertainties and increase the detection significance to $3 - 4\sigma$.

[4] The difference between bulge-to-disk flux and luminosity ratio is only important for our home Galaxy and is related to the fact that the Sun is located within the galactic radius. For external galaxies this difference disappears since their bulge and disk appear at the same distance to us.

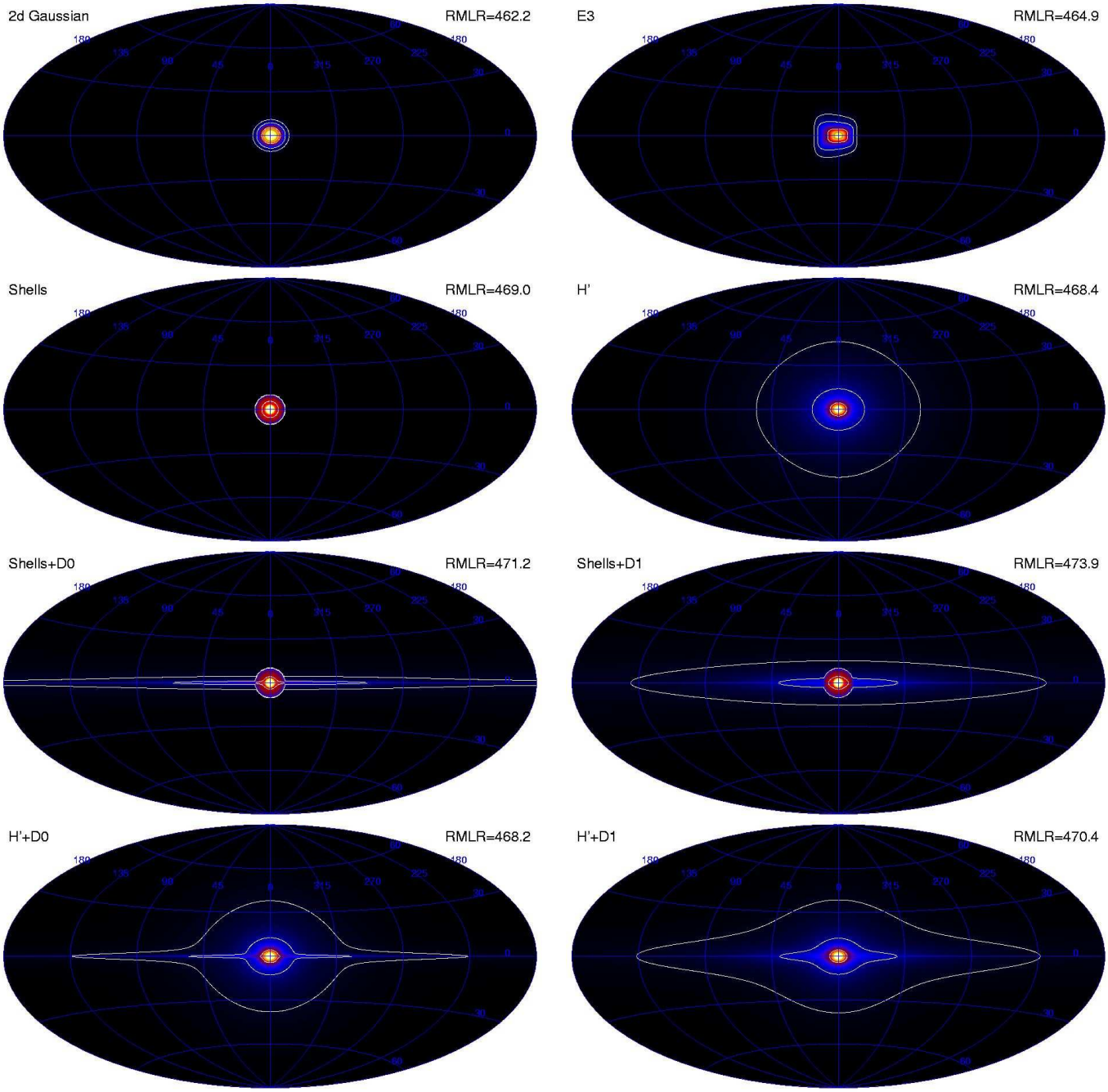

Fig. 8. All-sky maps of the best fitting models of 511 keV gamma-ray line emission (see text for a description of the models). Contour levels indicate intensity levels (from the centre outwards) of 10^{-2}, 10^{-3}, and 10^{-4} ph cm^{-2}s^{-1}sr^{-1}. The resulting RMLRs of the model fits are quoted in the upper-right corner of the panels.

The tracer maps used for the comparison are those listed in Knödlseder et al. (1999b). For a detailed description of the maps the reader is referred to that work.

Figure 9 summarises the result of the correlation study for our 511 keV dataset, where we show the RMLR as a function of the tracer map (ordered by increasing photon energy or decreasing wavelength). None of the tracer maps is consistent with the data. The maximum RMLR that is reached (353.7 for the DIRBE 2.2 μm map) is more than 100 units smaller than the values obtained for the parametric models of the previous sections. Apparently, the 511 keV emission morphology is unique and cannot be represented by any known celestial intensity distribution.

Nevertheless, Fig. 9 shows a clear trend, where the data favour maps in the near-infrared domain (DIRBE 1.25 μm - 4.9 μm) and the hard X-ray band (HEAO-1) over maps observed at longer wavelengths. In particular, the worst fits are obtained in the microwave and far-infrared domain where the skymaps trace the young stellar population, either through their ionising radiation (DMR maps at $\nu \gtrsim 53$ GHz), or through their related molecular gas (CO) and cold dust emission (DIRBE 100 μm - 240 μm).

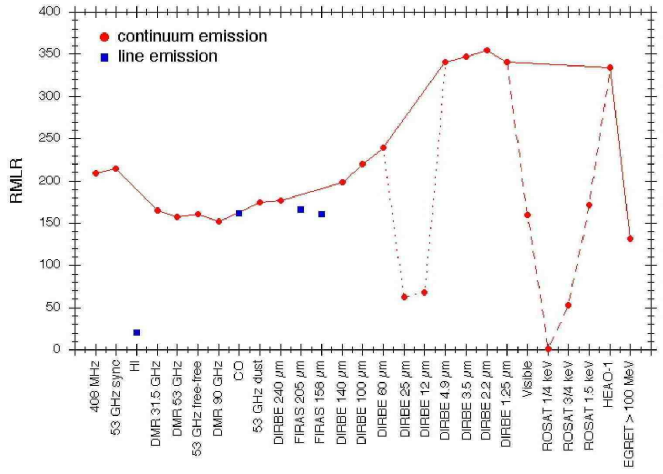

Fig. 9. Reduced maximum log likelihood-ratio (RMLR) as function of the tracer map, ordered by increasing photon energy (or decreasing wavelength). The dotted line illustrates the impact of zodiacal light contamination in the DIRBE 12 μm and 25 μm skymaps, the dashed line indicates maps that are heavily affected by galactic absorption.

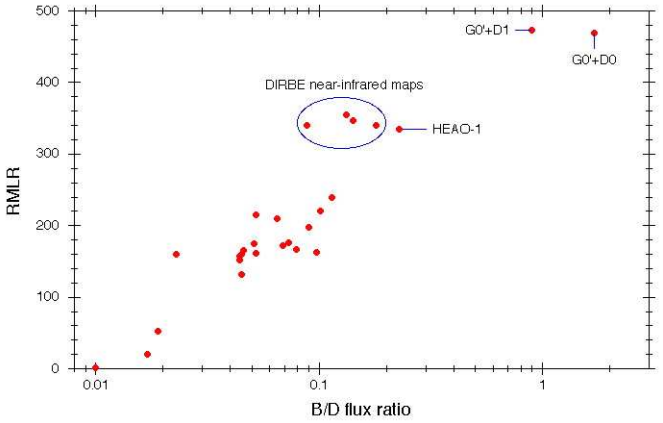

Fig. 10. Reduced maximum log likelihood-ratio (RMLR) as function of the bulge-to-disk flux ratio of the tracer map. The results for the parametric bulge+disk models are also shown.

From this it is clear that the bulk of the 511 keV emission is not related to the young massive stellar population of the Galaxy.

On the contrary, all best fitting tracers maps show the characteristic features of an old stellar population: a strong bulge component combined with a short scale radius disk component. Apparently, the 511 keV data tend to favour such morphologies. This is illustrated in Fig. 10 where we plot the RMLR as function of the bulge-to-disk flux ratio of the tracer map, defined as the flux contained within a circular region of 6° in radius around the galactic centre, divided by the flux within galactic latitudes $b = \pm 20°$ outside the circular bulge region (note that the precise B/D value depends of course on the exact definitions chosen for the two regions, but our purpose here is to illustrate a trend). Clearly, there is a strong correlation between the B/D flux ratio and the RMLR, in the sense that the larger the B/D flux ratio, the larger the RMLR. In particular, the DIRBE near-infrared maps and the HEAO-1 map show the largest B/D flux ratios of all tracer maps (~ 0.2). Thus, finding a population of objects which show a large B/D ratio could provide the key for finding the galactic source of positrons.

4.4. Point-source search

The modest angular resolution of SPI of about 3° (Vedrenne et al. 2003) makes it difficult to distinguish between point source, point-like, and small-scale diffuse emission. So in principle we cannot exclude the possibility that the 511 keV gamma-ray line emission that is seen towards the galactic bulge region is made of a limited number of point sources that blend to simulate diffuse emission. In due course the question of any point source contribution to the flux will be best addressed using data from the imager IBIS on INTEGRAL, which is relatively insensitive to diffuse emission, in conjunction with that from SPI. Such work is underway and will be reported on separately. We here limit ourselves to the constraints which can be placed from SPI data alone on such a contribution.

We have therefore used the SPIROS algorithm (Skinner & Connell 2003) to search our dataset for the positions and fluxes of point sources that are compatible with our data. SPIROS searches for the most probable position for a point source and fits a source at that position before repeating iteratively the search using the residuals after sources already found are taken into account. At each iteration the positions and fluxes of all sources that have been found are optimised by maximising a goodness of fit parameter (the χ^2 statistic was used here).

If the 511 keV emission is intrinsically diffuse then application of this algorithm will lead to sources being placed at selected positions (regions of high flux and local noise peaks) until a distribution of emission is found that is consistent (given limited statistics) with the data. Such a description is unlikely, however, to be unique and if most or all of the flux is from diffuse emission then the particular source positions found will have no astrophysical significance. We therefore do not present here the detailed results of this blind source search and we restrict ourselves to discussion of the general conclusions which can be drawn from the analysis.

For models with 7 point sources based on the SPIROS solution after iteration 7 we obtain RMLR = 462.5, slightly inferior to our best fitting diffuse models. Subsequent iterations suggest point sources at the edge of the exposed regions which are obviously spurious. Only after iteration 13 is another point source found in the galactic bulge region. Fitting this source together with the 7 sources found earlier leads to RMLR = 471.9, comparable

to the best fitting diffuse models. The total flux attributed to the 8 point sources is 1.1×10^{-3} ph cm^{-2}s^{-1}, comparable with the values obtained for the bulge component using our best fitting diffuse models (c.f. Table 2). We therefore simply conclude that at least 8 point sources would be needed to satisfactorily describe the SPI data.[5]

In addition to the blind search for point sources, we also looked for evidence of 511 keV gamma-ray line emission from a list of potential candidate objects. Our list comprises compact objects, pulsars, supernova remnants, star forming regions, globular clusters, nearby (active) galaxies, and galaxy clusters. Depending on the expected source extent, we searched for either point source emission or extended emission, modelled by a 2d angular Gaussian surface brightness distribution for which we specify the centroid and the FWHM extension.

The results of the analysis are summarised in Table 4. None of the sources we searched for showed a significant 511 keV flux, hence we only quote (3σ) upper limits in Table 4. Since the emission of the Galaxy may interfere with the emission from the specific sources (due to the large field of view of the SPI instrument), we also included models for the diffuse galactic 511 keV emission for the source search. We have used combinations Shells+D0, Shells+D1, H'+D0 and H'+D1 to cover the range of plausible best fitting diffuse models (c.f. Fig. 8) and quote always the most conservative flux limit. The (less sensitive) `ORBIT-DETE` background model has been used to ensure that systematic uncertainties are negligible.

5. Discussion

5.1. Comparison with earlier measurements

Observations of the 511 keV line emission have been made by a large number of balloon and satellite borne telescopes, yet only a few of them provided constraining information on the emission morphology. The OSSE instrument that flew during 1991-2000 on-board CGRO accumulated so far the largest database for studying the 511 keV line intensity distribution. The observations of the Gamma-Ray Spectrometer on-board the Solar Maximum Mission (SMM) (1980-1988) and of the Transient Gamma-Ray Spectrometer (TGRS) on-board the WIND mission (1995-1997) have also been used to estimate the overall 511 keV line flux and maximum emission size (Purcell et al. 1994; Kinzer et al. 1996; Tueller et al. 1996; Cheng et al. 1997; Purcell et al. 1997; Harris et al. 1998; Milne et al. 2000; Kinzer et al. 2001).

The picture that emerged prior to the INTEGRAL launch was the following. From the general trend that instruments with larger fields-of-view show larger fluxes it was inferred that the 511 keV emission is extended. OSSE observations strongly exclude a single point-source located at the GC (Purcell et al. 1994). The OSSE observations suggest at least two emission components, one being a spheroidal bulge and the other being a galactic disk component. A third component, named the Positive Latitude Enhancement (PLE), situated about $9^\circ - 12^\circ$ above the GC has been reported (Cheng et al. 1997; Purcell et al. 1997), but the morphology and intensity of this component was in fact only poorly determined by the data (Milne et al. 2000).

Table 5. Comparison of SPI results with OSSE measurements. The bulge parameters l_0, b_0, Δl, and Δb of OSSE were taken from Kinzer et al. (2001).

Quantity	SPI	OSSE
l_0	$-0.6^\circ \pm 0.3^\circ$	$-0.25^\circ \pm 0.25^\circ$
b_0	$+0.1^\circ \pm 0.3^\circ$	$-0.3^\circ \pm 0.2^\circ$
Δl (FWHM)	$8.1^\circ \pm 0.9^\circ$	$6.3^\circ \pm 1.5^\circ$
Δb (FWHM)	$7.2^\circ \pm 0.9^\circ$	$4.9^\circ \pm 0.7^\circ$
Flux (10^{-3} ph cm^{-2}s^{-1})	$1.5 - 2.9$	$1 - 3$
B/D flux ratio	$1 - 3$	$0.2 - 3.3$

The emission, which showed no significant offset from the GC, was well fitted by either a model comprising a narrow ($5 - 6^\circ$ FWHM) Gaussian bulge plus $\sim 35^\circ$ FWHM Gaussian and CO-like disk components, or by a centre-truncated $R^{1/4}$ spheroid plus exponential disk model (Purcell et al. 1997; Milne et al. 2000; Kinzer et al. 2001). The total 511 keV gamma-ray line flux was estimated to be $(1 - 3) \times 10^{-3}$ ph cm^{-2}s^{-1}. The distribution of flux between the bulge and disk components was only weakly constrained by the observations, and depended sensitively on the assumed bulge shape. In particular, estimates for the bulge-to-disk (B/D) flux ratio varied from $0.2 - 3.3$ depending upon whether the bulge component features a halo (which leads to a large B/D ratio) or not (Milne et al. 2000).

Our analysis basically confirms the pre-INTEGRAL observations (c.f. Table 5). One difference is that the bulge appears slightly larger in our analysis when compared to the OSSE result. We note that OSSE performed differential measurements using its $4^\circ \times 11^\circ$ collimator which may bias the results towards small values (Kinzer et al. 2001), but in any case, the discrepancy is not very significant and is not surprising in view of possible systematic uncertainties.

Another difference with respect to OSSE is that we find no evidence for a feature resembling the PLE. Fitting a model of the PLE (2d Gaussian of 5° FWHM located at $l = -2^\circ$ and $b = 8^\circ$) on top of the bulge results in a 3σ upper flux limit of 1.5×10^{-4} ph cm^{-2}s^{-1} for the PLE. The OSSE team has gradually reduced their estimates of the flux and significance attributed to this emission feature from 5×10^{-4} ph cm^{-2}s^{-1} (Purcell et al. 1997) down to an upper limit of 1×10^{-4} ph cm^{-2}s^{-1} (Milne et al. 2001). Recently it has been suggested that data analysis problems linked with variable continuum emission may

[5] Given the angular resolution of SPI, compact sources with an extent $\sim 1^\circ - 2^\circ$ would be considered as point sources in this context.

Table 4. 511 keV narrow line 3σ upper flux limits for selected potential positron sources.

Source name	l (deg)	b (deg)	FWHM (deg)	3σ flux limit (10^{-4} ph cm^{-2}s^{-1})	Type of object
Sgr A*	0.00°	+0.00°	-	< 1.0	BHC
GRS 1758-258	4.51°	−1.36°	-	< 0.7	μQSO
Cyg X-1	71.33°	+3.07°	-	< 1.0	BHC
LS I+61°303	135.68°	+1.09°	-	< 3.3	μQSO
1E 1740.7-2942	359.15°	−0.12°	-	< 0.9	μQSO
Vela X-1	263.06°	+3.93°	-	< 1.1	HMXB
GX 5-1	5.08°	−1.02°	-	< 0.7	LMXB
GRS 1915+105	45.37°	−0.22°	-	< 1.0	LMXB
A 0620-00	209.96°	−6.54°	-	< 3.8	LMXB
Nova Muscae	295.30°	−7.07°	-	< 2.0	LMXB
Cir X-1	322.12°	+0.04°	-	< 1.1	LMXB
Cen X-4	332.24°	+23.89°	-	< 1.7	LMXB
GX 349+2	349.10°	+2.75°	-	< 0.8	LMXB
Sco X-1	359.09°	+23.78°	-	< 1.5	LMXB
Crab	184.56°	−5.78°	-	< 1.3	Pulsar
Geminga	195.13°	+4.27°	-	< 2.2	Pulsar
PSR J0737-3039	245.24°	−4.50°	-	< 3.0	Pulsar
Kepler	4.52°	+6.82°	-	< 0.7	SNR
Cas A	111.73°	−2.13°	-	< 1.9	SNR
Tycho	120.07°	+1.44°	-	< 2.0	SNR
SN 1987A	279.70°	−31.94°	-	< 1.0	SNR
SN 1006	327.58°	+14.59°	-	< 1.3	SNR
Lupus Loop	329.80°	+16.00°	-	< 1.3	SNR
Cygnus	79°	0°	5°	< 1.8	Star forming region (^{26}Al source)
Vela	265°	0°	5°	< 2.6	Star forming region (^{26}Al source)
Carina	286.5°	+0.5°	-	< 2.2	Star forming region (^{26}Al source)
M 22	9.89°	−7.55°	-	< 0.8	Globular Cluster
Palomar 13	87.10°	−42.70°	-	< 7.0	Globular Cluster
ω Cen	309.10°	+14.97°	-	< 1.7	Globular Cluster
NGC 6397	338.16°	−11.96°	-	< 1.2	Globular Cluster
M 4	350.97°	+15.97°	-	< 1.1	Globular Cluster
Sgr dwarf	5.61°	−14.10°	8°	< 1.7	Dwarf Galaxy
M31	121.17°	−21.57°	3°	< 11.8	Galaxy
LMC	280.47°	−32.89°	10.8°	< 4.7	Irregular Galaxy
QSO B2251-179	46.20°	−61.33°	-	< 2.9	QSO
3C 273	289.95°	+64.36°	-	< 1.2	QSO
3C 279	305.10°	+57.06°	-	< 1.3	Blazar
Cen A	309.52°	+19.42°	-	< 1.7	Radio Galaxy
Coma cluster	58.08°	+87.96°	4°	< 2.0	Galaxy Cluster
Perseus cluster	150.58°	−13.26°	4°	< 4.5	Galaxy Cluster
Virgo cluster	281.63°	+75.18°	12°	< 2.5	Galaxy Cluster

account for the reported PLE (Milne 2004), so perhaps our non-detection of a PLE feature is not surprising.

Until now, there have been very few published upper limits on 511 keV gamma-ray line emission from point sources which take account of diffuse emission. Examples are the 3σ limits of 1.6×10^{-4} ph cm^{-2}s^{-1} for 1E 1740.7-2942 (Purcell et al. 1994) and $\sim 1.4 \times 10^{-4}$ ph cm^{-2}s^{-1} for inner Galaxy sources (Milne et al. 2001). Our upper limits, summarised in Table 4, are somewhat more stringent.

Finally, we want to mention that the method of analysis used in this work assumes that the 511 keV line emission is not time variable. From our analysis of SPI data alone we have no indications for time variability. Furthermore, OSSE and TGRS measurements revealed no significant time variability (Purcell et al. 1997; Harris et

al. 1998) and in addition, our 511 keV line flux measurements are consistent with those of OSSE and TGRS. Thus we believe that our assumption of non-variable 511 keV line emission is reasonable. We have, however, not yet performed a thorough analysis on all relevant timescales.

5.2. General considerations

The most distinctive morphological feature of the 511 keV emission is the large B/D luminosity ratio of $3-9$. Unless there is a mechanism that strongly suppresses positron annihilation in the galactic disk, or that somehow transports positrons from the disk into the galactic bulge or halo where they annihilate, the positron source population we are seeking for should also exhibit such a high B/D ratio.

The B/D luminosity ratio of $3-9$ is considerably larger than the B/D mass ratio of $0.3-1.0$ of our Galaxy (e.g. Caldwell & Ostriker 1981; Freudenreich 1998; Bissantz & Gerhard 2002; Robin et al. 2003). The uncertainty in the galactic B/D mass ratio is partly due to differences in the modelling of the disk component, where disk profiles exhibiting a central hole or depletion lead to B/D ratios at the high end, while double exponential profiles without hole favour B/D ratios at the low end. Since we employed in our analysis disk models with central holes from Robin et al. (2003), we should for consistency compare our 511 keV B/D luminosity ratio to their (large) B/D ratio of ~ 1.[6] But even with such large B/D mass ratios, the source population we are seeking for should still be at least 3 times more abundant in the bulge than in the disk of the Galaxy. We therefore conclude that the primary positron source of the Galaxy is clearly associated with the galactic bulge. It therefore should belong to the old stellar population.

Furthermore, the fact that the 511 keV emission matches well the morphology of the stellar bulge suggests that positron diffusion probably plays only a minor role. Were positron diffusion to be important we would expect to find substantial 511 keV emission in gas-rich regions adjacent to the rather gas-poor galactic bulge, such as the molecular ring structure at galactocentric distances of ~ 4 kpc. However, we do not find any evidence for 511 keV emission correlated with this structure. We therefore conclude that positron diffusion is negligible at galactic scales (i.e. kpc scales).

5.3. Constraints on the disk source

One certain source of positrons in the disk of the Galaxy is the radioisotope ^{26}Al. It decays with a lifetime of $\tau \sim 10^6$ yr with emission of a 1809 keV gamma-ray photon; $\sim 85\%$ of the decays are also accompanied by the emission of a positron. The galactic distribution of ^{26}Al is well known thanks to observations of the COMPTEL telescope aboard CGRO, and follows that of the young stellar population. Thus, under the assumption that the positrons annihilate close to their production site, 511 keV line emission along the galactic plane is expected, showing the morphological characteristics of a young stellar population.

The expected 511 keV line flux F_{511} due to ^{26}Al decay is related to the 1809 keV line flux F_{1809} through $F_{511} = 0.85 \times (2 - 1.5 f_{\rm p}) \times F_{1809}$. Using the COMPTEL measurement of the 1809 keV flux along the galactic plane, $F_{1809} = 9 \times 10^{-4}$ ph cm^{-2}s^{-1} (c.f. Table 4.3 in Knödlseder 1997), and assuming $f_{\rm p} = 0.93$ leads to an expected 511 keV line flux of $F_{511} = 5 \times 10^{-4}$ ph cm^{-2}s^{-1}.

Fitting our model of the young stellar population (model D0), together with bulge models to the data suggests a disk flux in the range $(4-6) \times 10^{-4}$ ph cm^{-2}s^{-1}. To explore the sensitivity of the disk flux on the assumed disk model we also paired the shell model with tracers of 1809 keV line emission, such as the DMR free-free and the DIRBE 240 μm emission maps (Knödlseder et al. 1999b). This resulted in slightly larger (and more significant) disk fluxes of $(8.3 \pm 2.3) \times 10^{-4}$ ph cm^{-2}s^{-1}. Comparing these values to what we expect from ^{26}Al suggests that $60-100\%$ of the galactic plane emission may be attributed to β^+-decay of ^{26}Al.

If this contribution is subtracted a 511 keV disk flux of at most $\sim 3 \times 10^{-4}$ ph cm^{-2}s^{-1} remains to be explained by other positron sources. A possible candidate is the radioisotope ^{44}Ti whose daughter isotope ^{44}Sc decays via β^+-decay into stable ^{44}Ca ($\tau \sim 87$ yr). In contrast to ^{26}Al there is no firm measurement of the present day galactic ^{44}Ti mass (nor of its spatial distribution), but simple chemical evolution arguments lead to the expectation that about 4×10^{-6} $M_\odot$ of ^{44}Ti are produced per year (Leising & Share 1994). Under the assumption that all positrons escape the production site this yield translates into an annihilation rate of 3×10^{42} s^{-1}. Assuming further that ^{44}Ti is distributed following model D0, a 511 keV disk flux of $\sim 8 \times 10^{-4}$ ph cm^{-2}s^{-1} is expected. In view of the approximate estimation and in particular in view of the uncertainty about the spatial distribution this value seems in reasonable agreement with the remaining 511 keV flux of $\sim 3 \times 10^{-4}$ ph cm^{-2}s^{-1}.

It is intriguing that the galactic disk flux could be entirely explained by the radioactive decay of ^{26}Al and ^{44}Ti. This would suggest that once the ^{26}Al and ^{44}Ti contributions have been subtracted only the bright bulge component of 511 keV emission remains, which would then demand a specific source population that is only confined to the inner Galaxy. However, we cannot immediately draw this conclusion. Fitting an old stellar population disk model, with larger scale height and smaller radial scale than the young one, increases the estimate of the disk flux by about a factor of two, leaving room for a weak disk component not associated with ^{26}Al or ^{44}Ti. This would suggest lower limits on the B/D flux (luminosity) ratio of $\gtrsim 2$ ($\gtrsim 6$) for the source population that gives rise to the galactic bulge emission.

[6] We note that, independently, large B/D ratios are also favoured by microlensing surveys towards the galactic bulge region (Binney & Evans 2001).

5.4. Constraints on the bulge source

5.4.1. Massive stars, core collapse supernovae, pulsars

The bulge dominance of the 511 keV emission immediately excludes scenarios in which the bulk of galactic positron production is related to massive stars. Such scenarios include the production of β^+-decay radioisotopes produced by Wolf-Rayet stars and all types of core collapse supernovae (including hypernovae) and the pair production in the strong magnetic fields of pulsars. Massive stars may well explain the faint disk component of 511 keV emission via the radioactive decay of ^{26}Al and ^{44}Ti (c.f. section 5.3). They cannot, however, explain the majority of the emission, which would in that case resemble the 1809 keV line emission.

5.4.2. Hypernovae

Cassé et al. (2004) proposed that a recent hypernova at the galactic centre could be responsible for the observed positron emission, but there is no observational evidence that such an explosion indeed took place. Hypernovae are believed to be related to Wolf-Rayet stars, which are distributed in the galactic disk following the spiral arm pattern, hence it would be much more likely to find a recent hypernova at an arbitrary position along the galactic plane (or at the tangent points of the spiral arms) rather than at the position of the galactic centre. And even in the rare event of a hypernova exploding right at the galactic centre, it would be difficult to explain why the resulting 511 keV annihilation radiation (arising from the β^+-decay of freshly synthesised ^{56}Co) should reflect the stellar morphology of the galactic bulge. We therefore conclude that it is unlikely that galactic centre hypernovae are the source of the bulge positrons.

5.4.3. Cosmic-ray interactions

Interactions of cosmic-ray particles with the ambient interstellar medium may produce positrons, primarily via the $\mathrm{N} + \mathrm{p} \rightarrow \pi^+ \rightarrow \mathrm{e}^+$ reaction channel (N stands for nucleus). The effect of the cosmic-ray interaction is best seen in the GeV gamma-ray domain, and has been comprehensively mapped by the EGRET satellite aboard CGRO. The EGRET all-sky map shows dominant emission from the galactic plane, which follows a linear combination of various gas and dust tracers in the galaxy. Thus cosmic-ray interactions should also lead to disk dominated 511 keV emission, which is at odds with our observations.

5.4.4. X-ray binaries

Positron production in X-ray binaries may occur either as a result of $\gamma\gamma$ pair production in the luminous compact region around the compact object or due to nuclear interactions that may form excited nuclei that subsequently decay through the emission of positrons. Galactic black holes and microquasars, where the positrons are ejected in a relativistic jet with Lorentz factors of a few (Dermer & Murphy 2001), are the two leading candidates.

X-ray binaries are separated into two classes, depending on whether the donor is a high-mass star (HMXB) or a low-mass star (LMXB). The two classes show clearly different spatial distributions (Grimm et al. 2002). HMXB are associated with the young stellar population and are primarily found in the galactic disk. Consequently they can immediately be excluded as the source of the bulge positrons. LMXB, in contrast, are strongly concentrated towards the galactic bulge, and are more promising source candidates. Among the 150 LMXBs listed in the catalogue of Liu et al. (2001), more than 50% are observed towards the galactic bulge. Correcting for completeness, Grimm et al. (2002) find a B/D ratio of ~ 0.9 and a vertical scale height of 410 pc for the LMXB distribution.

Formally, the LMXB B/D ratio is considerably below the value required by our 511 keV data, yet the large vertical scale height of LMXB could lead to a scenario where a substantial fraction of positrons from disk LMXB may escape into the galactic halo. This scenario works as follows. Since the scale height of LMXB (410 pc) considerably exceeds the scale height of the dense interstellar gas layer of our Galaxy ($\sim$ 100 pc), positrons from disk LMXB are ejected into rather low-density regions, typically a factor of $10 - 100$ less dense than regions found near the galactic plane (Ferrière 1998). Before positrons can annihilate they have to slow down considerably, mostly through Coulomb interactions, with a characteristic timescale of $\tau_{\mathrm{SD}} \sim 10^5 n^{-1}$ yr, n being the ISM density in units of cm^{-3} (Forman et al. 1986). Consequently, positrons live $10 - 100$ times longer at large scale heights than near the galactic plane, allowing for substantial diffusion before annihilation takes place. The typical diffusion length depends much on the magnetic field configuration and the amount of ISM turbulence at large scale heights, but qualitatively it seems plausible that a considerable fraction of the disk positrons may annihilate in the galactic halo.

The resulting broad diffuse component of 511 keV emission would be difficult to detect with SPI. In particular, the present dataset, for which good exposure is restricted to a band $b \lesssim \pm 15^\circ$ along the galactic plane (c.f. Fig. 1), makes it virtually impossible to measure a disk component with a broad-latitude distribution of 511 keV emission. Therefore it would be sufficient that $\sim 2/3$ of the positrons produced by disk LMXB escape into the galactic halo to reconcile the LMXB distribution with a B/D ratio of 3. If we require a more extreme B/D ratio of 6, as expected after subtraction of the ^{26}Al component from the disk (c.f. section 5.3), a positron escape fraction of $\sim 80\%$ would be needed for disk LMXB. It remains to be seen whether such large escape fractions are feasible.

An alternative way to test the LMXB scenario is to search for 511 keV line emission from individual bright and/or nearby objects. So far no emission is seen towards the interesting candidates Sco X-1 (the brightest LMXB)

and Cen X-4 and A0620-00 (probably the most nearby LMXB at ~ 1.2 kpc), but we plan for deep observations of these objects in the near future to search for their annihilation signatures. The detection of positron annihilation signatures from nearby objects could however be hampered by (even modest) positron diffusion away from the sources, which would lead to extended 511 keV emission halos around the objects. So even for the modest angular resolution of SPI of $\sim 3°$ nearby individual LMXB could appear as extended sources, and their low surface brightness could make their detection more difficult.

5.4.5. Classical novae

Among all proposed positron candidate sources, classical novae, i.e. thermonuclear runaways on white dwarfs in accreting binary systems, are the sources for which the largest B/D ratios of $\sim 3-4$ have been suggested (Della Valle & Duerbeck 1993; Della Valle & Livio 1994a). Interstellar extinction, in particular towards the galactic bulge region, makes it virtually impossible to derive their spatial distribution in the Milky Way directly, but novae are readily observed in nearby external galaxies which may serve as templates (e.g. Shafter et al. 2000). Due to its proximity and due to its similarity to the Milky Way, M31 is the primary source of information, and modern investigations indicate that novae reside primarily in the bulge region of M31 (Ciardullo et al. 1987; Capaccioli et al. 1989). Although it had been suggested that selection effects may have "faked" such a finding (Hatano et al. 1997) the recent study of Shafter & Irby (2001) demonstrates that such biases, if they exist, must be small.

Novae produce positrons via the β^+-decay of radioactive isotopes synthesised during the thermonuclear runaway, mainly of ^{13}N, ^{18}F, and ^{22}Na (lifetimes $\tau = 14$ min, 2.6 hr, and 3.75 yr, respectively). ^{22}Na yields of 6×10^{-9} $M_\odot$, as suggested by theoretical nucleosynthesis calculations for ONe novae (Hernanz et al. 2002), would require nova rates of ~ 1600 yr^{-1} to maintain positron production and annihilation in an equilibrium state, a rate which is considerably above estimates of 35 ± 11 yr^{-1} for all types of novae in the entire Galaxy (Shafter 1997). ^{13}N yields of 2×10^{-7} $M_\odot$ for low-mass CO novae are more promising (Hernanz et al. 2002) since they would require nova rates of only 26 yr^{-1} if all positrons could indeed escape from the nova envelope into the ISM. However, with a ^{13}N lifetime of 14 min it seems unlikely that this would be possible.

It is probable that large fractions of the ^{13}N positrons annihilate within the dense nova envelope, leading to prompt annihilation that could give rise to transient annihilation signatures (Leising & Clayton 1987; Gómez-Gomar et al. 1998). This signature has been sought using various gamma-ray telescopes, but has so far eluded detection (see Hernanz & José 2004 and references therein). Detection of the transient signature may help to shed light on the positron escape fraction, and could show whether novae contribute to the galactic bulge positron budget or not.

5.4.6. Thermonuclear supernovae

In view of their potential to produce large numbers of positrons, thermonuclear Type Ia supernovae (SN Ia) are often considered as the most plausible source of positrons in the Milky Way (Dermer & Murphy 2001). SN Ia produce positrons via the β^+-decay of radioactive ^{56}Co ($\tau = 111$ days). Expected ^{56}Co yields of ~ 0.6 $M_\odot$ provide $\sim 2.5 \times 10^{54}$ positrons per event, although, as with novae, prompt annihilation in the supernova envelope probably prevents large fractions of the positrons from escaping into the ISM. From the analysis of late light curves of SN Ia Milne et al. (1999) derive a mean escaped positron yield of $\sim 8 \times 10^{52}$ positrons per SN Ia, corresponding to a positron escape fraction of $f \sim 0.03$. A recent study of SN 2000cx even suggests $f \sim 0$, but SN 2000cx was an unusual event that may not represent the average SN in the bulge of our Galaxy (Sollerman et al. 2004).

Assuming therefore $f = 0.03$ a bulge SN Ia rate of 0.6 per century is required to maintain the observed 511 keV luminosity in a steady state. Unfortunately the rate and distribution of SN Ia in our Galaxy are only poorly known. The galactic SN Ia rate is generally inferred from rates observed in external galaxies which are then scaled to the mass and the type of the Milky Way. In that way rates of $0.3-1.1$ SN Ia per century are derived (Tammann et al. 1994; Cappellaro et al. 1997; Mannucci et al. 2005), sufficient to maintain the galactic 511 keV luminosity. In contrast, when we follow the suggestion of Prantzos (2004) and derive the bulge SN Ia rate by scaling the SN Ia rate observed in early-type galaxies to the mass of the galactic bulge, a bulge SN Ia rate of 0.08 SN Ia per century is obtained. This value is much too low to explain the observed bulge 511 keV luminosity. It is difficult to judge if the galactic bulge can indeed be considered as a downsized version of an elliptical galaxy, in particular in view of the differences in the evolution of the galactic bulge and an elliptical galaxy. Furthermore, it is suggested that different SN Ia explosion mechanisms exist in different types of galaxy (e.g. Della Valle & Livio 1994b; Howell 2001; Mannucci et al. 2005) making the proposed extrapolation even more uncertain.

Observations of external galaxies indicate that SN Ia distributions are strongly peaked towards galactic centres (Bartunov et al. 1992), yet reliable determinations of B/D ratios are difficult in view of observational biases and selection effects (Wang et al. 1997; Hatano et al. 1998; Howell et al. 2000). If the SN Ia distributions follows that of novae (both populations are believed to arise from accreting white dwarfs; see van den Bergh 1988) one can expect B/D ratios of $\sim 3-4$. Even higher B/D ratios can be achieved if part of the positrons produced by disk SN Ia, which have a vertical scale height of ~ 330 pc (Chen et al. 2001), escape into the halo (c.f. section 5.4.4). Thus SN Ia could

indeed present the required characteristics that are needed to explain the positron distribution and annihilation rate in the Galaxy.

Alternatively, instead of explaining the bulge emission globally we may search for 511 keV emission from nearby Type Ia supernovae remnants, such as SN 1006, the Lupus Loop, or the Tycho SNR. Assuming a mean escaped positron yield of $\sim 8 \times 10^{52}$ positrons per SN Ia (Milne et al. 1999) and a positronium fraction of $f_{\rm p} = 0.93$, the mean expected 511 keV line flux from an individual SN Ia is estimated to

$$F_{511} = 1.3 \times 10^{-4} \left(\frac{1 \text{ kpc}}{D}\right)^2 \left(\frac{10^5 \text{ yr}}{\tau}\right) \text{ ph cm}^{-2}\text{s}^{-1} \quad (9)$$

where D is the distance to the supernova remnant in units of kpc, and τ is the mean lifetime of the positrons in years, between $10^3 - 10^7$ yr, depending on the density, temperature, and ionisation state of the annihilating medium (Guessoum et al. 1991). Taking distances of $D \sim 2$ kpc for SN 1006 (Laming et al. 1996), of $D \sim 1$ kpc for the Lupus Loop (Leahy et al. 1991), and of $D \sim 2.3$ kpc for Tycho (Hughes 2000) and assuming a positron lifetime of 10^5 yr results in predicted 511 keV line fluxes of 0.3×10^{-4} ph cm^{-2}s^{-1}, 1.3×10^{-4} ph cm^{-2}s^{-1}, and 0.2×10^{-4} ph cm^{-2}s^{-1}, respectively. At least for the Lupus Loop, the predicted flux is close to our upper 511 keV flux limit, indicating that dedicated deep observations of nearby supernova remnants can help to answer the question about the galactic positron source. Such dedicated observations with INTEGRAL are already scheduled.

5.4.7. Light dark matter annihilation

Light dark matter (1-100 MeV) annihilation, as suggested recently by Boehm et al. (2004), is probably the most exotic but also the most exciting candidate source of galactic positrons. Unfortunately, the spatial distribution of dark matter in general, and light dark matter in particular, is only poorly constrained by observational data, at least for the inner Galaxy. The debate of whether the dark matter profile shows a cusp towards the galactic centre is still not settled, but it seems clear now that, dynamically, dark matter plays only a minor role in the inner 3 kpc of the Galaxy. In this region the stellar mass dominates (Binney & Evans 2001; Klypin et al. 2002).

Due to these uncertainties it is difficult to judge whether the observed 511 keV emission could be explained by dark matter annihilation. Maybe more promising is the idea to search for signatures of dark matter annihilation in nearby, external galaxies. Hooper et al. (2004) suggested that nearby dwarf spheroidal galaxies may provide prominent sources of 511 keV line emission due to the high densities of dark matter that are known to be present. They proposed the nearby Sagittarius dwarf galaxy (Sgr dwarf) as most promising candidate and estimate 511 keV line fluxes in the range of $(1-7) \times 10^{-4}$ ph cm^{-2}s^{-1}, depending on the assumed dark matter halo profile. Cordier et al. (2004) searched for emission from this Galaxy using SPI and obtained a (3σ) upper limit of 3.8×10^{-4} ph cm^{-2}s^{-1}. Our upper limit of 1.7×10^{-4} ph cm^{-2}s^{-1} is substantially lower, and excludes almost all types of halo models for this galaxy, in particular those with a central cusp.

Standard cold dark matter cosmology predicts cuspy dark matter distributions (Klypin et al. 2002), so in principle Sgr dwarf should have been detected by SPI if dark matter annihilation were a viable scenario. Maybe dark matter halos are less cuspy than theory predicts? This possibility is indeed indicated by observations of our own Galaxy (Binney & Evans 2001) and dwarf galaxies (Blais-Ouellette et al. 1999; Kleyna et al. 2003). But in this case dark matter annihilation should not lead to a compact but to a rather extended 511 keV emission feature – in contradiction to what SPI observations of the inner Galaxy suggest. From the arguments given one may question the dark matter scenario. However, it is certainly premature to reject them totally because of the uncertainties in the dark halo profiles and the annihilation conditions.

6. Conclusions

Our first mapping of 511 keV gamma-ray line emission over a large fraction of the celestial sphere leads us to the following observations:

1. 511 keV emission is significantly ($\sim 50\sigma$) detected towards the galactic bulge region, and, at a very low level ($\sim 4\sigma$), from the galactic disk
2. there is no evidence for a point-like source in addition to the diffuse emission, down to a typical flux limit of $\sim 10^{-4}$ ph cm^{-2}s^{-1}
3. there is no evidence for the positive latitude enhancement that has been reported from OSSE measurements; the 3σ upper flux limit for this feature is 1.5×10^{-4} ph cm^{-2}s^{-1}
4. the bulge emission is spherically symmetric and is centred on the galactic centre with an extension of $\sim 8°$ (FWHM); it is equally well described by models that represent the stellar bulge or the halo populations
5. the bulge annihilation rate is $(1.5 \pm 0.1) \times 10^{43}$ s^{-1}, the disk annihilation rate is $(0.3 \pm 0.2) \times 10^{43}$ s^{-1}
6. the bulge-to-disk luminosity ratio lies in the range $3-9$

The bulge dominated 511 keV line emission morphology suggests an old stellar population as the main galactic positron source. In contrast, the faint disk emission is well explained by the release of positrons during the radioactive decay of ^{26}Al that originated from massive stars, with a possible contribution from ^{44}Ti synthesised during supernova explosions.

The extreme bulge-to-disk ratio that is observed in the 511 keV luminosity imposes severe constraints on the principal galactic positron source. Type Ia supernovae, low-mass X-ray binaries or dark matter annihilation may possibly satisfy these constraints, but uncertainties in the

knowledge about the spatial distribution of these objects and the positron escape processes prevents us from drawing firm conclusions. Novae could probably most easily explain the large B/D ratios, yet an implausibly large positron escape fraction from ^{13}N decay would be required to accommodate the observed annihilation rate. SN Ia could explain the annihilation rate for a modest positron escape fraction, but it is questionable if they have the required large B/D ratio. LMXB could reproduce the observed B/D ratio provided that a substantial fraction of positrons ejected by disk LMXB escape into the halo. Light dark matter is an exciting option, but it remains to be seen if the observed 511 keV emission distribution is compatible with the profile of the galactic dark matter halo.

Future deep observations of individual nearby candidate sources may provide the means to identify the galactic positron source. As such we will soon observe the X-ray binaries Sco X-1 and Cen X-4 with INTEGRAL, and observations of the nearby supernova remnant SN 1006 are already scheduled. We cannot be sure that any of these observations will allow the detection of a 511 keV signal, but were such a signal detected we would gain important new insights in the primary source of positrons in our Galaxy.

Appendix A: Summary of galactic density profiles

Bulge models: We model the galactic bulge as a triaxial stellar bar for which the parameters are summarised in Table A.1. The apparent intensity distribution on the sky is computed in the galactic frame which we define by a right-handed cartesian coordinate system where the Sun is located on the negative y-axis, at $-R_\odot = 8.5$ kpc. The transformation from the galactic frame into the bar frame is performed by two consecutive rotations: the first, represented by the matrix $R_X(\alpha)$, is a counterclockwise rotation by an angle α around the z-axis; the second, represented by the matrix $R_Y(-\beta)$, is a clockwise rotation by an angle β around the new y-axis, i.e.

$$\boldsymbol{r'} = R_Y(-\beta)R_X(\alpha)\boldsymbol{r} \tag{A.1}$$

The effective bar radius is defined by

$$R_\mathrm{s} = \left(\left[\left(\frac{|x'|}{a_\mathrm{x}} \right)^{C_\perp} + \left(\frac{|y'|}{a_\mathrm{y}} \right)^{C_\perp} \right]^{\frac{C_\parallel}{C_\perp}} + \left(\frac{|z'|}{a_\mathrm{z}} \right)^{C_\parallel} \right)^{\frac{1}{C_\parallel}} \tag{A.2}$$

where a_x, a_y, and a_z are the scale lengths and $C_\perp$ and $C_\parallel$ are the face-on and the edge-on shape parameters. The radial dependencies of the bar density are given by various density profiles that we designate by labels:

$$\mathrm{G}: \ \rho_\mathrm{G} = \ \rho_0 \times f_\mathrm{max}(R_\mathrm{xy}) \times \exp(-0.5 R_\mathrm{s}^2) \tag{A.3}$$

$$\mathrm{G3}: \ \rho_\mathrm{G3} = \ \rho_0 \times f_\mathrm{max}(R_\mathrm{xy}) \times R_\mathrm{s}^{-1.8} \exp(-R_\mathrm{s}^3) \tag{A.4}$$

$$\mathrm{E}: \ \rho_\mathrm{E} = \ \rho_0 \times f_\mathrm{max}(R_\mathrm{xy}) \times \exp(-R_\mathrm{s}^n) \tag{A.5}$$

$$\mathrm{E3}: \ \rho_\mathrm{E3} = \ \rho_0 \times f_\mathrm{max}(R_\mathrm{xy}) \times K_0(R_\mathrm{s}) \tag{A.6}$$

$$\mathrm{S}: \ \rho_\mathrm{S} = \ \rho_0 \times f_\mathrm{max}(R_\mathrm{xy}) \times \mathrm{sech}^2(R_\mathrm{s}) \tag{A.7}$$

$$\mathrm{P}: \ \rho_\mathrm{P} = \ \rho_0 \times f_\mathrm{max}(R_\mathrm{xy}) \times [1 + (R_s/R_c)]^{-1} \tag{A.8}$$

where

$$f_\mathrm{max}(R_\mathrm{xy}) = \begin{cases} 1.0 & \text{for } R_\mathrm{xy} \leq R_\mathrm{max} \\ \exp\left(-\frac{1}{2} \left(\frac{R_\mathrm{xy} - R_\mathrm{max}}{a_\mathrm{max}} \right)^2 \right) & \text{for } R_\mathrm{xy} > R_\mathrm{max} \end{cases} \tag{A.9}$$

is a cutoff function and

$$R_\mathrm{xy} = \sqrt{x^2 + y^2} \tag{A.10}$$

is the distance from the galactic centre in the xy-plane.

Model D0: For the young disk population we use the model proposed by Robin et al. (2003) to describe the young (age < 0.15 Gyr) stellar disk population of the Galaxy:

$$\rho(x, y, z) = \rho_0(\exp(-(a/R_0)^2) - \exp(-(a/R_i)^2)) \tag{A.11}$$

where

$$a^2 = x^2 + y^2 + z^2/\epsilon^2. \tag{A.12}$$

This model presents a truncated exponential disk profile with a fixed disk axis ratio of $\epsilon = 0.014$, a fixed disk scale radius of $R_0 = 5$ kpc, and a fixed inner disk truncation radius of $R_i = 3$ kpc. The vertical exponential scale height of the disk is $z_0 = 70$ pc.

Model D1: For the old disk population we use the model proposed by Robin et al. (2003) to describe the old (age $7 - 10$ Gyr) stellar disk population of the Galaxy:

$$\begin{aligned} \rho(x, y, z) \ = \ & \rho_0(\exp(-(0.25 + a^2/R_0^2)^{1/2}) - \\ & \exp(-(0.25 + a^2/R_i^2)^{1/2})) \end{aligned} \tag{A.13}$$

This model presents a truncated exponential disk profile with a fixed disk axis ratio of $\epsilon = 0.0791$, a fixed disk scale radius of $R_0 = 2.53$ kpc, and a fixed inner disk truncation radius of $R_i = 1.32$ kpc. The vertical exponential scale height of the disk is $z_0 = 200$ pc.

Model H: To model the stellar halo we use the general model proposed by Robin et al. (2003):

$$\rho(R, z) = \rho_0(a/R_\odot)^{-n} \tag{A.14}$$

where a is defined by Eq. A.12 (the flatness of the model is set by the value of the axis ratio ϵ in Eq. A.12), and $a \geq a_c$, avoiding a singularity at the galactic centre. n determines the slope of the density profile.

Model S: A set of galactocentric nested spherical shells of constant density. The radii of the shells and their number has been varied in order to maximise the MLR, while using the minimum number of shells required to satisfactorily describe the data.

Acknowledgements. The SPI project has been completed under the responsibility and leadership of CNES. We are grateful to ASI, CEA, CNES, DLR, ESA, INTA, NASA and OSTC for support.

Table A.1. Parameters of the triaxial galactic bulge models used in this work (see text).

Model	α	β	a_x	a_y	a_z	$C_\perp$	$C_\parallel$	n	R_c	R_{max}	a_{max}
G0	0.0	0.0	0.91		0.51	2	2			∞	
G1	73.8	0.6	3.11	0.76	0.48	2	2			2.40	0.71
G2	70.7	0.8	1.56	0.60	0.45	2	4			2.40	0.71
G3	59.0	0.7	3.78	1.44	1.19	2	2			2.40	0.71
E0	0.0	0.0				2	1			∞	
E1	65.7	0.5	2.23	0.65	0.32	1	1			2.40	0.71
E2	49.0	0.6	0.75	0.19	0.27	2	2			2.40	0.71
E3	49.8	0.7	0.69	0.19	0.28	2	4			2.40	0.71
S_F	76.2	0.02	1.70	0.64	0.44	1.57	3.50			3.13	0.46
E_F	80.5	−0.05	1.89	0.66	0.43	1.61	3.49	1.44		3.57	0.56
P_F	76.8	0.02	1.81	0.65	0.43	1.65	3.02	5.04	1.23	2.71	0.88
S_{PR}	79.4	−0.8	1.87	0.56	0.47	3.49	3.38			3.71	

References

Bartunov, O. S., Makarova, I. N., & Tsvetkov, D. Yu. 1992, A&A, 264, 428

Binney, J. J., & Evans, N. W. 2001, MNRAS, 327, L27

Bissantz, N., & Gerhard, O. E. 2002, MNRAS, 330, 591

Blais-Ouellette, S., Carignan, C., Amram, P., & Coté, S. 1999, AJ, 118, 2123

Boehm, C., Hooper, D., Silk, J., et al. 2004, Phys. Rev. Letters, 92, 1301

Brown, B. L., & Leventhal, M. 1987, ApJ, 319, 637

Caldwell, J. A. R., & Ostriker, J. P. 1981, ApJ, 251, 61

Capaccioli, M., della Valle, M., Rosino, L., & D'Onofrio, M. 1989, AJ, 97, 1622

Cappellaro, E., Turatto, M., Tsvetkov, D. Yu., et al. 1997, A&A, 322, 431

Cash, W. 1979, ApJ, 228, 939

Cassé, M., Cordier, B., Paul, J., & Schanne, S. 2004, ApJ, 602, 17

Chen, B., Stoughton, C., Smith, J., et al. 2001, ApJ, 553, 184

Cheng, L. X., Leventhal, M., Smith, D. M., et al. 1997, ApJ, 481, L43

Churazov, E., Sunyaev, R., Sazonov, S., Revnivtsev, M., & Varshalovich, D. 2005, MNRAS, 357, 1377

Ciardullo, R., Ford, H. C., Neill, J. D., et al. 1987, ApJ, 318, 520

Clayton, D. D. 1973, Nature Phys. Sci., 244, 137

Clayton, D. D., & Hoyle, F. 1974, ApJ, 187, 101

Cordier, B., Attié, D., Cassé, M., et al. 2004, Proc. 5th INTEGRAL workshop (Munich), ESA SP-552, 581 (`astro-ph/0404499`)

Dearborn, D. S. P., & Blake, J. B. 1985, ApJ, 288, 21

Della Valle, M., & Duerbeck, H. W. 1993, A&A, 271, 175

Della Valle, M., & Livio, M. 1994a, A&A, 286, 786

Della Valle, M., & Livio, M. 1994b, ApJ, 423, L31

Dermer, C. D., & Murphy, R. J. 2001, Proc. 4th INTEGRAL workshop (Alicante), ESA SP-459, 115 (`astro-ph/0107216`)

Dwek, E., Arendt, R. G., Hauser, M. G., et al. 1995, ApJ, 445, 716

Ferrière, K. 1998, ApJ, 503, 700

Forman, M., Ramaty, R., & Zweibel, E. 1986, in Physics of the Sun, ed. P. Sturrock, p. 249

Freudenreich, H.T. 1998, ApJ, 492, 495

Gómez-Gomar, J., Hernanz, M., José, J., & Jean, P. 1998, MNRAS, 296, 913

Grimm, H. J., Gilfanov, M., & Sunyaev, R. 2002, A&A, 391, 923

Guessoum, N., Ramaty, R., & Lingenfelter, R. E. 1991, ApJ, 378, 170

Harris, M. J., Teegarden, B. J., Cline, T. L., et al. 1998, ApJ, 501, L55

Hatano, K. 1997, MNRAS, 290, 113

Hatano, K., Branch, D., & Deaton, J. 1998, ApJ, 502, 177

Hernanz, M., Gómez-Gomar, J., & José, J. 2002, New Astronomy Reviews, 46, 559

Hernanz, M., & José, J. 2004, New Astronomy Reviews, 48, 35

Hooper, D., Ferrer, F., Boehm, C., et al. 2004, Phys. Rev. Lett, 93, 1302

Howell, D. A., Wang, L., & Wheeler, J. C. 2000, ApJ, 530, 166

Howell, D. A. 2001, ApJ, 554, L193

Hughes, J. P. 2000, ApJ, 545, L53

Jean, P., Knödlseder, J., Lonjou, V., et al. 2003a, A&A, 407, L55

Jean, P., Vedrenne, G., Roques, J.-P., et al. 2003b, A&A, 411, L107

Johnson, W. N., & Haymes, R. C. 1973, ApJ, 184, 103

Kaufman, L. 1987, IEEE Trans. Med. Img., 6, 37

Kinzer, R. L., Purcell, W. R., Johnson, W. N., et al. 1996, A&AS, 120C, 317

Kinzer, R. L., Milne, P. A., Kurfess, J. D., et al. 2001, ApJ, 559, 282

Kleyna, J. T., Wilkinson, M. I., Gilmore, G., & Evans, W. 2003, ApJ, 588, L21

Klypin, A., Zhao, H., & Somerville, R. S. 2002, ApJ, 573, 597

Knödlseder, J. 1997, PhD thesis, Univ. Paul Sabatier, Toulouse

Knödlseder, J., Dixon, D., Bennett, K., et al. 1999a, A&A, 345, 813

Knödlseder, J., Bennett, K., Bloemen, H., et al. 1999b, A&A, 344, 68

Knödlseder, J., Lonjou, V., Jean, P., et al. 2004a, A&A, 411, 457

Laming, J. M., Raymond, J. C., McLaughlin, B. M., & Blair, W. P. 1996, ApJ, 472, 267

Leahy, D. A., Nousek, J., & Hamilton, A. J. S. 1991, ApJ, 374, 218

Leising, M. D., & Clayton, D. D. 1987, ApJ, 323, 159

Leising, M. D., & Share, G. H. 1994, ApJ, 424, 200

Leventhal, M., MacCallum, C. J., & Stang, P. D. 1978, ApJ, 225, L11
Lingenfelter, R. E., & Hueter, G. J. 1984, in: High-Energy Transients in Astrophysics, ed. S. E. Woosley, AIP Conference Proceedings, 558
Liu, Q. Z., van Paradijs, J., & van den Heuvel, E. P. J. 2001, A&A, 368, 1021
Lonjou, V., Knödlseder, J., Roques, J.-P., et al. 2004, Proc. 5th INTEGRAL workshop (Munich), ESA SP-552, 129
Lucy, L. B. 1974, AJ, 79, 745
Mannucci, F., Della Valle, M., Panagia, N., et al. 2005, A&A, 433, 807
Milne, P. A., The, L.-S., & Leising, M. 1999, ApJS, 124, 503
Milne, P. A., Kurfess, J. D., Kinzer, R. L., Leising, M. D., & Dixon, D. D. 2000, AIP Conference Proceedings, 510, 21
Milne, P. A., Kurfess, J. D., Kinzer, R. L., & Leising, M. D. 2001, AIP Conference Proceedings, 587, 11
Milne, P. A. 2004, New Astronomy Reviews, 48, 93
Norgaard, H. 1980, ApJ, 236, 895
Picaud, S., & Robin, A.C. 2004, A&A, 428, 891
Prantzos, N. 2004, Proc. 5th INTEGRAL workshop (Munich), ESA SP-552, 15
Purcell, W. R., Grabelsky, D. A., Ulmer, M. P., et al. 1994, in Proc. Second Compton Symp., eds. C. Fichtel, N. Gehrels, and J. Norris (New York: AIP), 403
Purcell, W. R., Cheng, L.-X., Dixon, D. D., et al. 1997, ApJ, 491, 725
Ramaty, R., Stecker, F. W., & Misra, D. 1970, J. Geophys. Res., 75, 1141
Ramaty, R., & Lingenfelter, R. E. 1979, Natur, 278, 127
Richardson, W. H. 1972, J. Opt. Soc. Am., 62, 55
Robin, A. C., Reylé, C., Derrière, S., & Picaud, S. 2003, A&A, 409, 523
Robin, A. C., Reylé, C., & Crézé, M. 2000, A&A, 359, 103
Roques, J.-P., Schanne, S., von Kienlin, A., et al. 2003, A&A, 411, 107
Rudaz, S., & Stecker, F. W. 1988, ApJ, 325, 16
Shafter, A. W. 1997, ApJ, 487, 226
Shafter, A. W., Ciardullo, R., Pritchet, C. J. 2000, ApJ, 530, 193
Shafter, A. W., & Irby, B. K. 2001, ApJ, 563, 749
Skinner, G., & Connell, P. 2003, A&A, 411, 123
Sollerman, J., Lindhal, J., Kozma, C., et al. 2004, A&A, 428, 555
Strong, A. W. 1985, A&A, 150, 273
Sturrock, P. A. 1971, ApJ, 164, 529
Tammann, G. A., Löffler, W., & Schröder, A. 1994, ApJS, 92, 487
Teegarden, B., Watanabe, K., Jean, P., et al. 2005, ApJ, 621, 296
Teegarden, B., Jean, P., Weidenspointner, G., et al. 2004, Proc. 5th INTEGRAL workshop (Munich), ESA SP-552, 819
Tueller, J., Gehrels, N., Leventhal, M., Smith, D. M., & Purcell, W. R. 1996, A&AS, 120C, 369
Van den Bergh, S. 1988, Comm. Astrophys., 12, 131
Vedrenne, G., Roques, J.-P., Schönfelder, V., et al. 2003, A&A, 411, 63
Wang, L., Höflich, P., & Wheeler, J. C. 1997, ApJ, 483, L29
Weidenspointner, G., Lonjou, V., Knödlseder, J., et al. 2004, Proc. 5th INTEGRAL workshop (Munich), ESA SP-552, 133 (`astro-ph/0406178`)